# Spatially and Temporally Resolving Concentration and Temperature Profiles within a Fresh and a Thermally-Aged Monolith Catalyst

By

Osama Talib Shakir

A thesis
presented to the University of Waterloo
in fulfillment of the
thesis requirement for the degree of
Master of Applied Science
in
Chemical Engineering

Waterloo, Ontario, Canada, 2008

# AUTHOR'S DECLARATION

I hereby declare that I am the sole author of this thesis. This is a true copy of the thesis, including any required final revisions, as accepted by my examiners. I understand that my thesis may be made electronically available to the public

Osama Shakir

# Abstract

The ability to resolve reactions within a monolith spatially and temporally is key in developing reliable kinetic models, as well as in validating proposed reaction mechanisms. In this work, two techniques, IR-thermography and spatially-resolved capillary inlet mass spectrometry (SpaciMS), were used to measure temperature and gas-phase concentrations. Specifically, they were applied to monitor the axial distribution of temperature and concentration profiles during propylene oxidation over a $Pt/Al_2O_3$ monolith-supported catalyst. Also, the effect of thermally aging the catalyst on the temperature and concentration patterns observed was investigated.

During temperature programmed oxidation experiments, the data show that conversion of propylene began at the outlet, and a reaction front generated at the rear of the monolith traveled upstream, as a moving reaction zone, thereby creating a temperature wave pattern since the reaction is exothermic. The conversion was always complete downstream of this reaction zone at any point along the catalyst. When the reactor was cooled, the conversion of propylene started to drop, accompanied by a similar temperature wave pattern that traveled in the opposite direction (from upstream to downstream) and was attributed to a phenomenon known as wrong-way behavior.

Finally, thermally aging the catalyst led to a slower and more localized moving hot zone.

# Acknowledgments

All praise be to Allah who blessed me with the strength, knowledge and perseverance to complete this work.

I would like to express the deepest gratitude to my most beloved parents for their infinite support and encouragement. I could have never done this without you. I am forever in debt to you. I would also like to thank my two brothers and my sister for their uplifting motivation.

Furthermore, I would like to extend my most sincere thanks to Professor William Epling. I am privileged to having been his student and worked under his supervision. His high level of professionalism, invaluable advice, and endless guidance and support enabled me to proceed and complete my research. What I have learned from him are lessons and skills that I will carry with me and cherish for the rest of my life.

In addition, I would like to express my appreciation to Professors Ali El-Kamel and Robert Hudgins. I am highly appreciative for their insightful comments and the time they have taken to review and edit this work.

I would also like to acknowledge NSERC for funding and Cummins Inc. for providing the reactor.

Last but not least, I would like to thank all the people I have met with and those who became my friends, especially my labmates, for making this a memorable experience.

# Dedication

I dedicate this work to my beloved parents.

I also dedicate this work to Palestine, a country that lives in my soul.

# Table of Contents

# List of Figures

# CHAPTER 1: Introduction

## 1.1 Catalytic Reactor Design

Reactions that involve species in the gaseous phase diffusing and adsorbing on/over solid catalysts are a ubiquitous and well analyzed type of reaction that are in every-day use. For heterogeneous catalytic reactions in general, the most common type of reactor in use is the fixed bed reactor. Fixed bed reactors have been adequately described as the power horse of the process industry [1].

Fixed bed reactors could be broadly classified into randomly packed bed reactors (PBRs), and structured fixed bed reactors. Due to the 'ordered' nature of structured fixed bed reactors, greater control is possible over the homogeneity of the bed properties, as well as better predictability of the bed's performance from fundamental theoretical analysis of the hydrodynamics, transport processes, and kinetics occurring throughout. For those reasons, significant research and resources have been put into the development of new and improved structured fixed bed reactors over the past years, and there is a trend to manufacture custom structured beds for specific applications to replace the conventional PBRs.

Although there has been a shift in preference towards structured beds, the science of reactor design behind structured beds is subject to the same fundamental laws of thermodynamics, reaction engineering, and heat and mass transfer. Fixed bed reactors are integral in nature, and are mathematically represented by the ideal plug flow reactor (PFR) model, with variation in reaction along the space dimension [2].

In general, the reaction rate is dependent on concentration and temperature. For fixed bed reactors, the concentration of reactants decreases down the length of a reactor while heat is being simultaneously released or absorbed. Hence, the concentration and temperature profiles are not uniform down the length of the bed, as shown in Figure 1-1. As a result

the reaction rate varies with distance as well as concentration and temperature. For the case of unsteady-state operation, variation of all the mentioned parameters as a function of time has to be considered as well, complicating matters further.
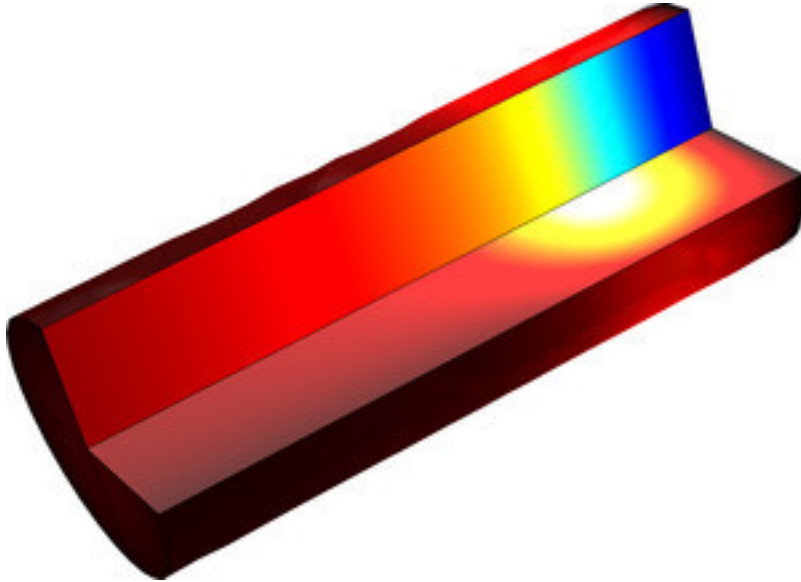


**Figure 1-1: A visualization of the non-uniform temperature profile along a plug flow reactor [3].**

In actual operation, a reactor's performance and efficiency are far from those predicted by ideal conditions. Furthermore, deactivation of the catalyst takes place over time, and for fixed beds, might take place at different regions with varying degrees, disturbing the uniformity of the activity distribution throughout the bed [4].

Detailed knowledge of reaction rate and transport process parameters is necessary for successful fixed bed reactor design. Such exact values, and accurate estimates of rate constants and driving forces for heat and mass, demand precise knowledge of temperature and concentration values at as many points down the length of the bed as possible. To obtain such data, experimental techniques and measurement tools that provide the data quickly as the reactions happen in real-time are needed. Such data are also necessary for complementing mathematical models aimed at efficient/accurate model development for catalytic reactor design.

## 1.2   The Monolith – A Structured Catalytic Bed

A type of structured catalytic bed that is being used in environmental applications, and is increasingly finding appeal in other areas, is the monolithic catalyst structure. The main advantages of monolith structures over other structured catalysts are [5]:

1- Low pressure drop, reducing upstream turbine operating costs.
2- Low sensitivity to plugging.
3- High mechanical strength, reducing demand for sophisticated frame structures.

Ceramics are most commonly used as the material for monolithic catalysts. Although one of the disadvantages of ceramic monoliths is their poor heat transfer properties, this can be overcome when necessary by using metallic monolith body structures.

The differences between reactor and catalyst diminish when discussing monoliths. Ceramic monoliths are typically made of cordierite and stainless steel for metallic monoliths [6]. Unless the monolith support is itself an active phase, or made from a highly porous material, the catalytically active phase is usually dispersed on a highly porous support, most commonly $\gamma$-$Al_2O_3$, which is in turn dispersed on the surface of the monolith support. The highly porous support, i.e. $Al_2O_3$, is called the wash-coat material. Figure 1-2 is a schematic showing an enlarged view of a typical catalytic monolith channel.
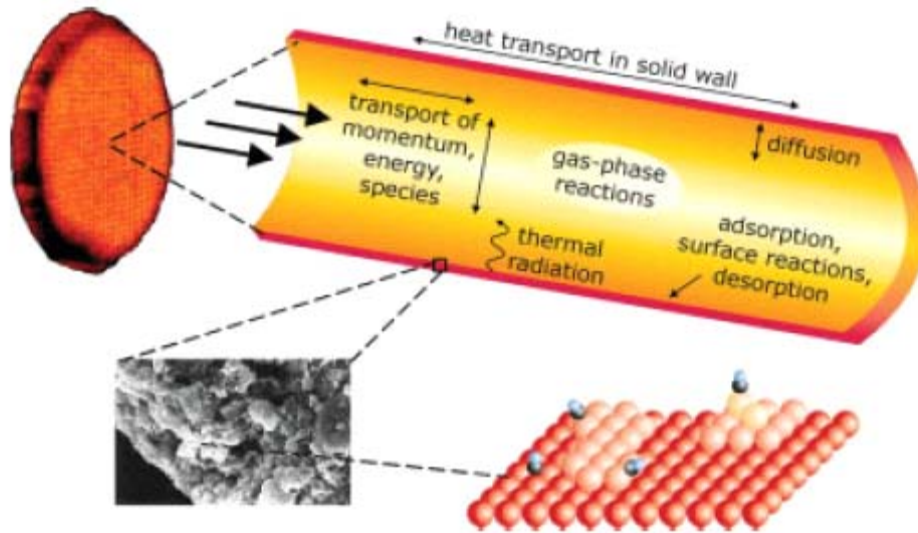
**Figure 1-2: Different views within a monolith channel and a visualization of the common processes occurring [50].**

## 1.3   Application of Monolithic Catalytic Reactors

Monolith catalysts were first used in decolorizing nitric acid tail gas and for control of automobile exhaust emissions [7]. After their proven success and feasibility, their use has become more general in fuel combustion exhaust and removal of harmful pollutants from industrial off-gases, although they are still finding increasing use in non-environmental applications. A new application is fuel combustion in the gas turbine cycle over a catalytic combustion catalyst [5]. Another non-conventional use of monolithic catalysts is their substitution in multiphase reactors, an application to-date being the hydrogenation of anthraquinone in the production of hydrogen peroxide [6].

The state-of-the-art in monolith reactor technology is the catalytic converter in automobile exhaust emission abatement. The composition and properties of the catalyst varies widely, depending on the oxygen content of the exhaust, which in turn depends on whether the source is a compression or spark ignition engine [8]. Catalytic converters are used to reduce the concentrations of three types of pollutants that are regulated by the EPA in gasoline-run engines. The three are hydrocarbons (HC), CO and NOx [9, 10], thus the converters are sometimes called three-way catalytic converters. HC and CO are oxidized, while reducing NOx emissions to $N_2$ [12]. While this has been achieved with

4

efficiencies in excess of 95% in oxygen-lean exhaust from spark ignition engines, the problem becomes more challenging in oxygen-rich exhaust, typical of compression ignition diesel fuel engines [6].

Being able to measure the extents and rates of the above redox reactions simultaneously in a single run in a monolithic catalytic converter is not a simple matter, particularly since the reaction mechanisms are naturally complicated and proceed in a sequence of stages that often occur at different regions within a channel, giving rise to non-uniform gradients, as well as non-uniform deactivation under sudden load increases and extreme operation. The existence of those gradients in both temperature and concentration are also motivation for optimizing the entire monolith composition as a function of position within the catalyst, or even on an individual channel basis [11].

An example of a catalytic converter where such gradients can be quite intense is the oxidizing catalyst installed upstream of NOx reducing catalysts in diesel engine exhaust, the diesel oxidation catalyst (DOC). These monolith-supported catalysts usually contain platinum as the active species because of its superior redox properties. The purpose of the DOC is to oxidize CO and HC. Also oxidation of NO into $NO_2$ is critical since $NO_2$ is a precursor species for reduction to $N_2$ in NOx storage and reduction (NSR) catalyst technology [13], or to partially oxidize the NO to achieve a 1:1 molar $NO:NO_2$ ratio in the gas stream for optimal performance of selective catalytic reduction (SCR) catalysts [12]. Overall, the DOC raises the efficiency of NOx reduction catalysts.

Steady state is rarely achieved during normal automobile operation, and fluctuations in inlet gas stream composition and temperature lead to a number of dynamic phenomena in the channels of a monolith. Such transient operation leads to moving reaction zones. The non steady-state behavior accentuates non-uniformity and can even lead to non-uniform deactivation of the catalyst. This is one more reason to study gradients and ultimately minimize degradation, and one way to do so is by optimizing or tailoring the catalyst loading or composition. In what follows, a particular catalytic converter technology for NOx control from mobile emissions will be discussed to highlight the points mentioned.

## 1.4 NOx Storage/Reduction – Inherent Gradients

Although a number of NOx abatement technologies have been proposed and applied, the major challenge common to all of them is carrying out the reduction reaction under predominantly oxidative conditions. One such technology is NOx Storage and Reduction (NSR). NSR catalytic converters are also monolith-supported, with a high surface area alumina wash-coat containing typically platinum and rhodium as well as an alkali or alkaline-earth compound. Platinum is used for the oxidation and reduction functions, while the alkali metal, usually barium or potassium, is the NOx storage component, forming nitrate species [13].

NSR technology is inherently transient. The process of reducing NOx occurs in a two-phase cycle; the lean phase and the rich phase. During the lean phase (lean in reductant relative to oxygen) the NOx gets stored on the basic sites of the catalyst. In the lean phase, the catalyst acts as a storage medium, and this continues for a measured length of time, up to a point when the storing capacity of the catalyst nears saturation. Just before NOx starts breaking through at the catalyst outlet, a switch is made in the inlet gas composition to the catalyst, to a phase rich in reductant, the rich phase. This phase lasts for just a few seconds, during which much of the NOx stored desorbs and is reduced to $N_2$. Figure 1-3 is a graph of the NOx concentration profile during these two phases.
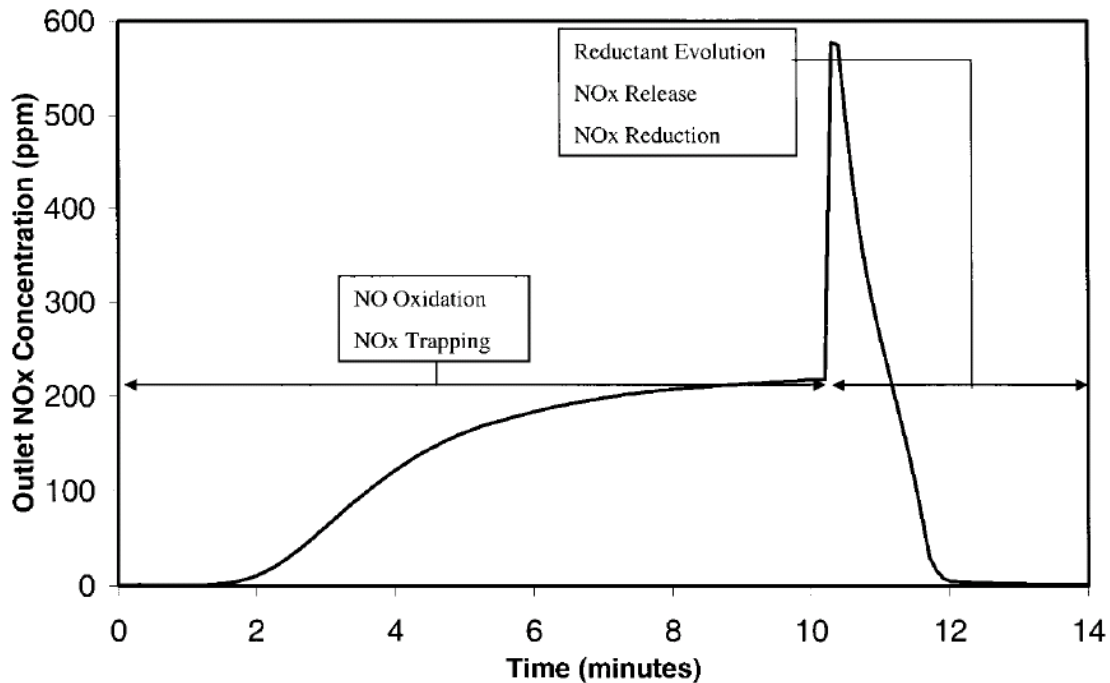
**Figure 1-3: Typical NOx outlet concentration profile versus time during one lean-rich cycle [13].**

As seen in Figure 1-3, during the lean or storage phase, all the NOx entering the catalyst is initially stored. Later, some NOx starts breaking through as the trapping sites are becoming saturated. The gases were switched to the rich phase after 10 minutes, where there was a spike in the NOx concentration indicating some of the NOx is released but not reduced.

The reduction of NOx in the NSR process proceeds in five steps [13]. These steps are:

1- NO oxidation to nitrogen dioxide ($NO_2$).
2- Sorption of NO or $NO_2$ on the surface as nitrates or nitrites.
3- Evolution of reductant on switching to rich phase.
4- NOx desorption from nitrite or nitrate sites.
5- NOx reduction to $N_2$.

In Figure 1-4, NOx breakthrough concentrations at four different axial points down a monolith channel are plotted as a function of time. This figure demonstrates the axial

7

variation in the concentration of NOx, which appears to be saturating the catalyst as a plug that moves downstream with time.
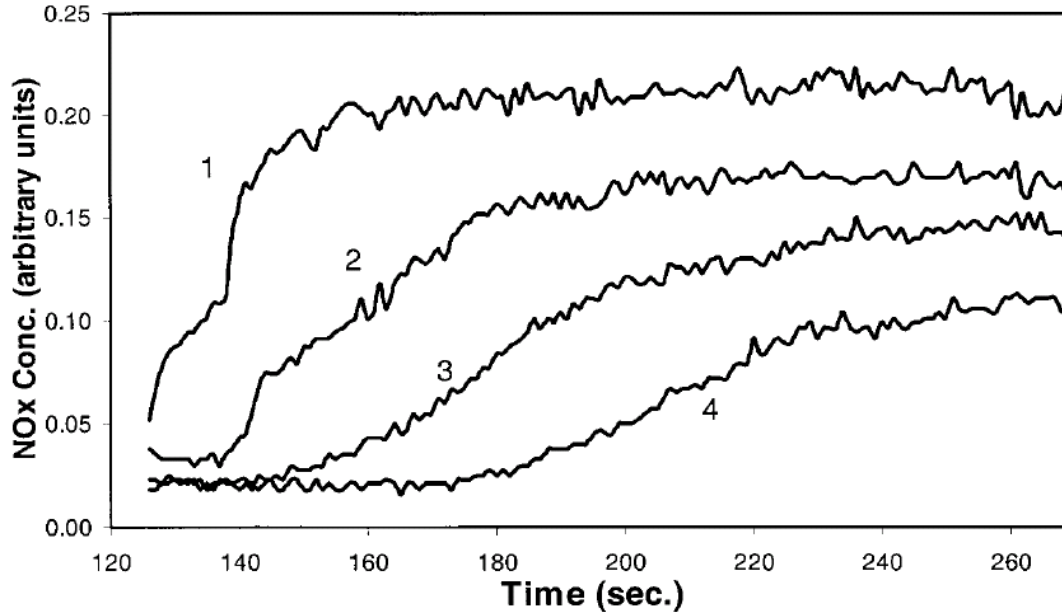


**Figure 1-4: NOx concentrations at different points along an NSR monolith catalyst [13].**

As shown in Figure 1-5, NOx storage is more efficient when $NO_2$ is the chemisorbing species rather than NO. NOx started slipping at the outlet earlier when NO was the inlet NOx species, compared to when $NO_2$ was the inlet NOx species. This is the purpose of step one in the five step sequence mentioned above. With this being the case, it is intuitive to assume that the first part of the monolith would be utilized in the oxidation reaction, whereas storage would become more effective downstream. Such a simple treatment highlights the fact that different regions in a monolith serve different functions, or at least serve the same function with different efficiencies. This is why interest arose in resolving the reactions and their kinetics along the channel in NSR catalysts, rather than treating it uniformly.
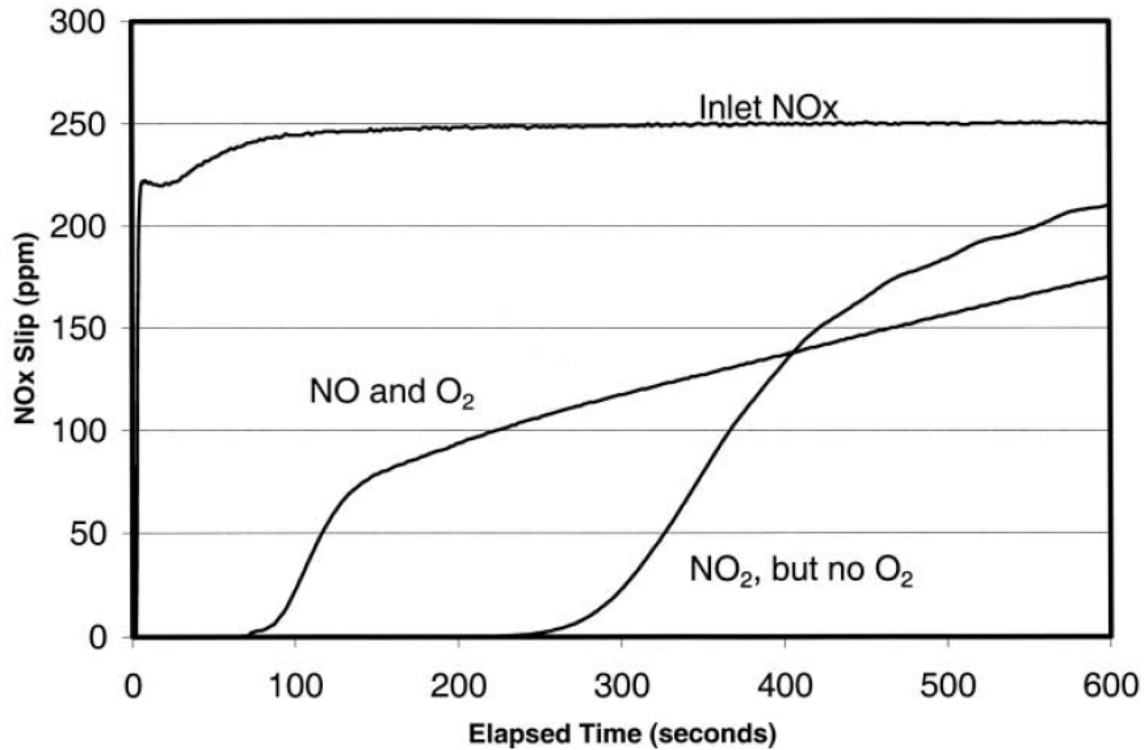
**Figure 1-5: Inlet and outlet concentration profiles for two different stream compositions. The first stream contains NO and oxygen. The second stream contains NO$_2$ only.**


In another study, the NOx storage and conversion was studied as a function of time and position for one storage and reduction cycle (56s/4s) with a Pt/K/Al$_2$O$_3$ catalyst [14]. The existence of gradients and strong dependencies on axial position were extensively discussed. In Figure 1-6, obtained from reference [14], the data shows that only the first quarter of the monolith was involved in storage, and the remaining not used.
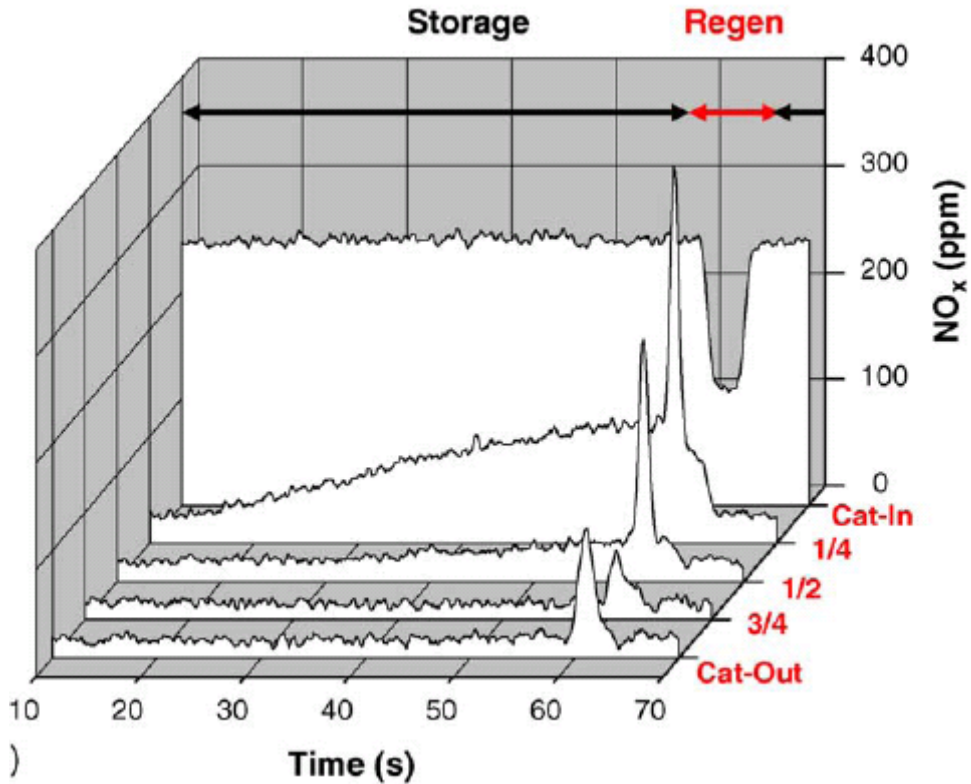
**Figure 1-6: NOx concentration profile as a function of time and dimensionless distance along the catalyst [14].**

Although the storage phase is the longer portion of the cycle, it is better understood than the quicker regeneration phase. The following figures, Figures 1-7 through 1-9, contain the data that shows the evolution of different species during a 4-second regeneration phase with CO as the reductant, to help understand the complex interactions between the species as a function of time and position.
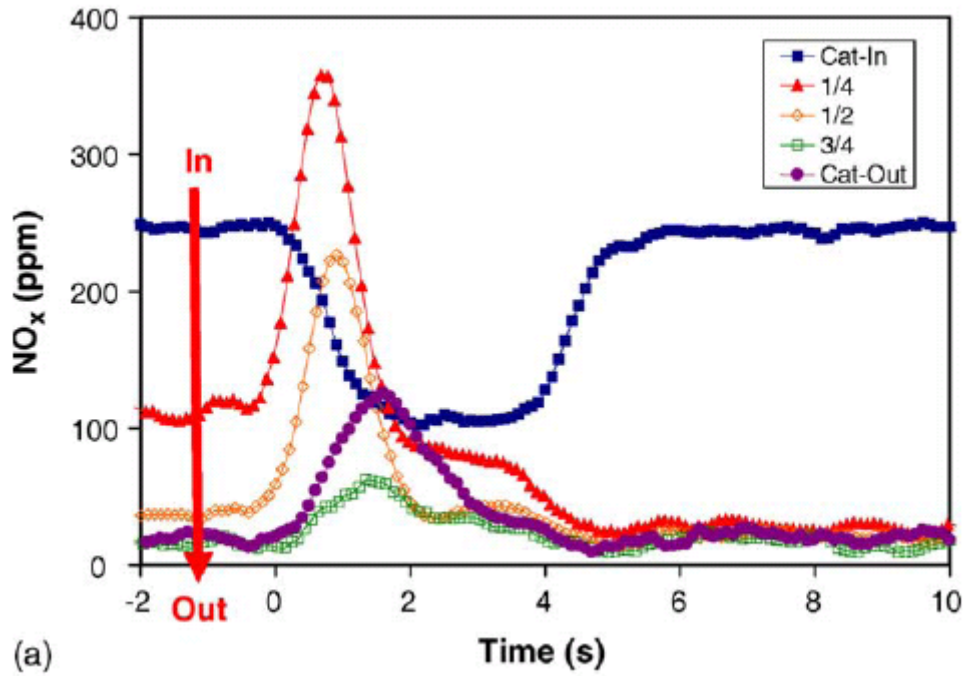
**Figure 1-7: NOx concentration versus time as a function of distance along the length of the NSR monolith catalyst [14].**
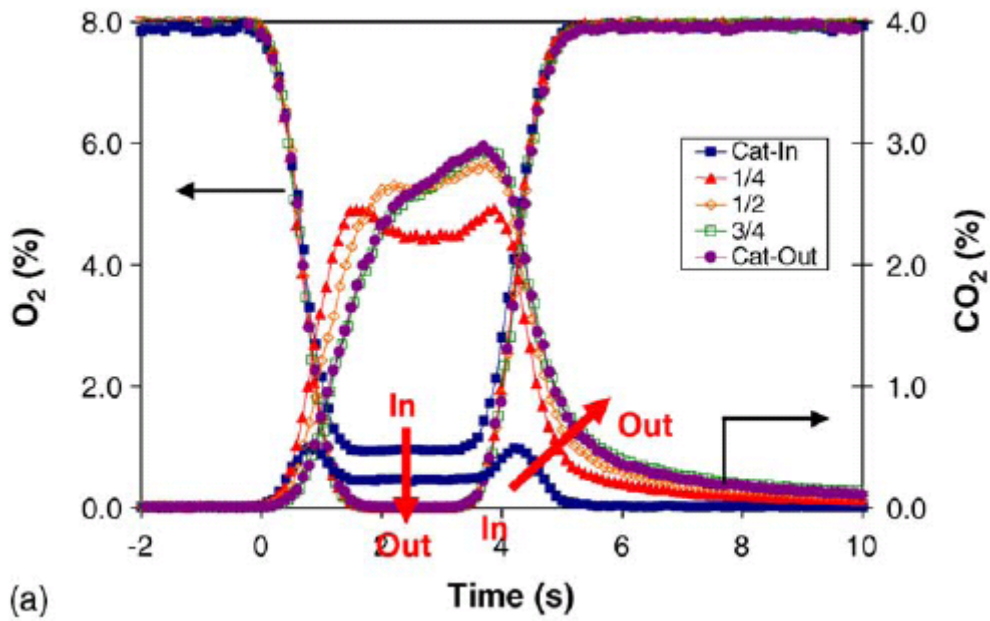


**Figure 1-8: Oxygen and CO₂ concentrations versus time as a function of distance along the length of the NSR monolith catalyst [14].**
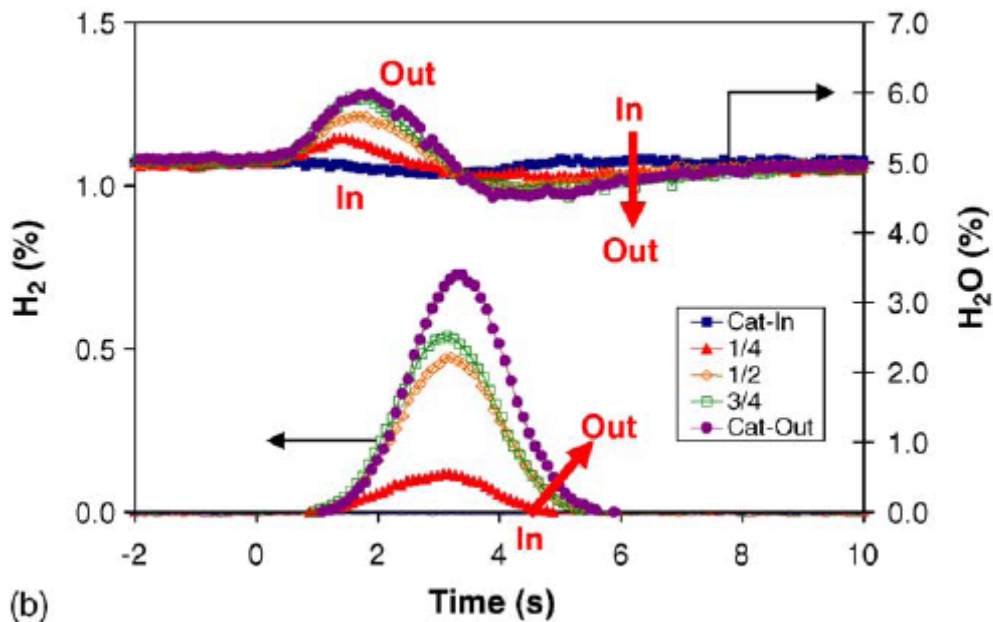
**Figure 1-9: Water and H₂ concentrations versus time as a function of distance along the length of the NSR monolith catalyst [14].**

These figures show the concentrations of the corresponding species just before, during and just after the regeneration phase. From Figure 1-7, it is apparent that the NOx release pattern matches that seen in Figure 1-6; the largest release occurring in the first quarter of the monolith, dropped further downstream, but with a larger amount measured at the outlet.

In Figure 1-8, multiple reactions contributed to the $O_2$ and $CO_2$ profiles, namely CO oxidation with residual oxygen from the storage phase and from the gas phase mixing front on switching between lean to rich, CO reaction with NOx, and the water gas shift (WGS) reaction. Although not immediately apparent from the graph, the oxidation of CO with oxygen occurred very quickly and was the dominant reaction within a narrow region at the inlet of the monolith. It was proven that all of this residual oxygen completely reacted with the CO, which was in excess within the first half of the catalyst. Hence $CO_2$ production at the second half of the catalyst was attributed to WGS, NOx reduction as well as reaction with surface-stored oxygen. In evaluating Figure 1-7, NOx was observed at different catalyst positions at different times, indicating that NOx reduction was indeed

12

occurring over the entire surface, and at progressively later times at downstream positions. However, there was not a monotonic decrease in the height of the NOx concentration peak, but rather the amount observed did decrease until the third quarter of the sample, when a larger peak was then measured at the outlet. From these data, along with FTIR data discussed indicating the presence of $NH_3$ at the outlet, it was concluded that the reduction of NOx proceeded in two steps which the authors termed primary and secondary. Primary reduction took place in regions limited in CO, resulting in $N_2$ as the major product. Secondary reduction took place over a different region in the monolith, rich in CO which was converted to $CO_2$ via the WGS reaction producing $H_2$ that reacted with the NOx and formed $NH_3$ as the major reduction product.

The reduction reaction of NOx by CO extended deep into the monolith. According to data in Figure 1-8, $O_2$ dropped from 8% to 1% at the inlet, but was completely absent at downstream positions. This led to the conclusion that although CO oxidation took place over the entire surface of the monolith with stored oxygen, additional oxidation took place in the front region of the catalyst because of oxygen in the mixing front on the switch from the lean to the rich phase.

With such gradients in concentrations, and one of the reactions being CO oxidation, there were accompanying gradients in temperature within the monolith. In Figure 1-10, the temperature profiles measured within one of the channels during a regeneration phase followed by the storage phase are shown.
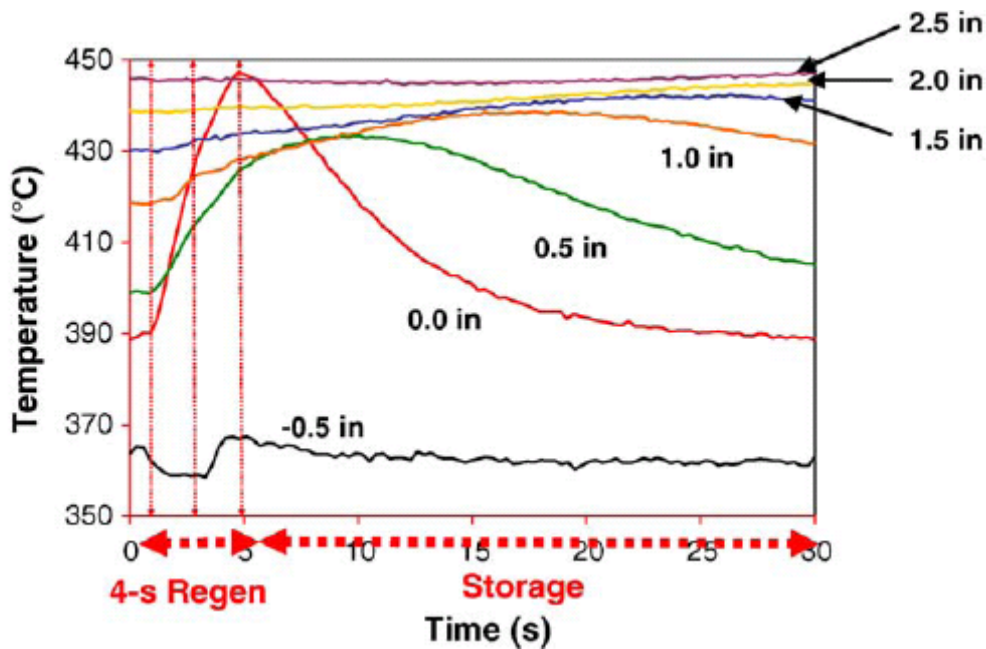
**Figure 1-10: Temperature profiles versus time at seven points down the length of the NSR monolith catalyst [14].**

A 50°C temperature difference was generated between the catalyst inlet and outlet during the regeneration phase. Coupling concentration speciation with temperature measurement led to the conclusion that there was a large exotherm generated very close to the inlet from the reaction of CO with stored residual oxygen as well as oxygen from the mixing front on the switch from lean to rich. Although the data showed that CO oxidation extended over the entire surface, more oxidation occurred at the front due to the presence of gas-phase oxygen from the mixing front. Further downstream however, the oxidation reaction of CO was only with residual surface oxygen and NOx. Thus smaller temperature changes were observed at downstream positions.

Overall, this is an example where a more complete understanding of the reactions was attained by spatially resolving the concentrations and temperatures.

# CHAPTER 2: Literature Review

## 2.1 Modeling Efforts

Engineers solve real life problems by employing the scientific method and mathematical tools to formulate the problem into a form amenable to numerical manipulation. By doing so, the problem is condensed into a numerical model whose parameters constitute the unique conditions of the problem, and is thus simplified. Devising a model with adjustable parameters enables us to locate the important factors that directly affect the system and refine our parameters to reach the best set of values that would give us the best representation of the situation at hand, or the best performance possible from the system. Monolithic catalysts and the axial set of reactions occurring within their channels represent exactly such a system that engineers attempt to model for predicting and optimizing performance.

The subject of asymmetry in space (axial direction) of fixed bed reactors during steady-state and dynamic operation has been the topic of study for many researchers. Variation in the axial coordinate has been observed over the years and exists in the form of sharp temperature and concentration gradients along the reactor's length. As these gradients were better understood, different names were given to the particular dynamic features, such as traveling hot spots, differential flow instability, and wrong-way behavior [15].

Luss [16] presented an excellent review of the experimental observations and theoretical predictions of spatio-temporal patterns on catalytic wafers and packed bed reactors. The focus was on hot zone formation, stationary or moving, which was considered the most relevant spatio-temporal phenomenon. The experimental observations reported were from catalytic wires and ribbons, catalytic rings and pellets, and from PBRs.

For PBRs, the review discussed axial temperature profiles as well as transversal (hot zones perpendicular to the direction of flow). Observed oscillatory behaviors were attributed to oscillatory and excitable reaction rates.

Within the same review, many earlier modeling-based papers were discussed. Although they indicated that it is difficult to find a general guideline for choosing a particular model for a system depending on the type of pattern formation, simulation efforts have been grouped into two main categories depending on the approach; reaction-diffusion systems, or reaction-convection-diffusion systems.

Hegedus [17] presented a mass-limited, one-dimensional and first order model to investigate the heat generation and distribution behavior characteristic of temperature excursions evolving across the length of a monolith. Oh and Cavendish [18] followed by simulating the transient behavior of a packed bed catalytic converter via its response to perturbations in inlet gas stream temperatures, using a one-dimensional two phase model. Yakhnin and Menzinger studied the formation and behavior of hot spot formation during $H_2$ combustion in monoliths, and the response to increasing gas flow velocities using a pseudo-1D model [19]. They found a relationship between the velocity of the gas stream and that of the reaction front, as well as the direction of propagation of the reaction front depending on the conditions. Sheintuch et al. [20] proposed a modified oscillatory elementary-step kinetic model to analyze the resulting spatiotemporal patterns during CO oxidation in a catalytic converter. Ramanathan et al. developed a detailed one-dimensional, two-phase model for a monolith catalyst with non-uniform loading, with which they performed bifurcation analysis [21], as well as an analysis of the light-off and cumulative emissions behavior [22]. A literature review of many previous modeling efforts was given in the former paper. Cybulski and Moujlin [23] and Groppi et al. [24] provided review articles that summarized the recent mathematical models that simulated heterogeneous monolith behavior. Although there is significant work and understanding of the dynamic behavior within a monolith via modeling, experiments designed to measure the transient variables and provide complimentary data to verify the simulation efforts are lacking.

## 2.2  Conventional Techniques

To supplement the modeling efforts and provide data that would validate or rebuke model predictions, techniques have been developed to monitor and measure such data. In this section, we mention some of the more conventional and earlier techniques employed for measuring spatial concentration and temperature distributions.

As would be expected, the method used to resolve reactant and product species concentrations within a reactor depends on the geometry and configuration of that reactor. For monolith reactors, most concentration measurements are obtained at the outlet due to difficulty of measurement access in the channels using the conventional techniques, which might be possible with other reactor configurations such as the ones mentioned below.

One example is the study of hydrocarbon combustion flames using Fourier transform reconstruction for emission transmission (E/T) IR spectra [25], in a combustion chamber, which is highly non-ideal with the presence of intense gradients. A method in which signals leading to 3-D images that enable spatial resolution of temperature and concentration profiles called Hadamard tomography has been demonstrated. The technique is based on soot particulates having poor transmittance (high absorbance and emittance). Soot is unburned carbon [26]. Basically, the combustion chamber is enclosed in the detection cell, and since detection is possible from multiple sides (angles), 3-D reconstruction of the temperature and concentration profiles is possible. This work is relevant to combustion studies, for either pollution control by monitoring soot composition, or for optimizing combustion by monitoring flame soot properties. However, this technique does not lend itself to use within structured reactor beds because of the fact that multiple laser sources would be necessary for irradiating each point within a channel for complete axial analysis.

Thermocouples have always been the conventional way to measure temperatures within monolith channels. The drawbacks of using thermocouples however are:

17

1- Slow response time.

2- Difficulty in knowing whether or not the thermocouple is in contact with the channel walls, and hence whether the solid or the gas temperature is what is being measured.

3- Axial conduction via the thermocouple body, convection from surrounding gas, and radiation to and from the junction, are difficult to account for.

Point number 2 is important since most of the time the temperature being measured is the gas-phase temperature, so for accurate kinetic parameter estimation, surface data needs to be obtained. Also, more often than not, the radiation losses from the thermocouple surface are not accounted for, further decreasing accuracy. However, due to the convenience of being able to locate them at any position within a channel, they have become very popular for that use. The issue of flow characteristic interference remains yet another issue.

A novel technique that was used to overcome the problem of tip conduction measurement broadening due to high thermal gradients, which reduces the accuracy of spatial resolution, is phosphor thermography, via phosphor-tipped fiber optics [27]. The insertion mechanism is similar to a thermocouple; however unlike a thermocouple; the temperature gradient stimulates phosphorescence which is then transmitted through the body of the fiber to a detector that relates the excitation lifetime of the phosphor to the local temperature, making it faster and more accurate.

The above is an overview of a few of the common techniques for concentration and temperature measurements. The techniques described however, have drawbacks, and are not readily applicable to spatial resolution inside a monolith channel. For this particular application, two techniques that have been developed and used successfully were combined, and they are discussed below.

## 2.3  IR Thermography

All bodies with temperatures above absolute zero emit radiation in all regions of the electromagnetic spectrum with varying intensities according to Planck's law of black-body radiation [28]:

$$E_\lambda d\lambda = \frac{2\pi c^2 h \lambda^{-5}}{e^{(ch/\lambda kT)} - 1} d\lambda \tag{1}$$

A plot of the above equation as a function of temperature would look as follows:
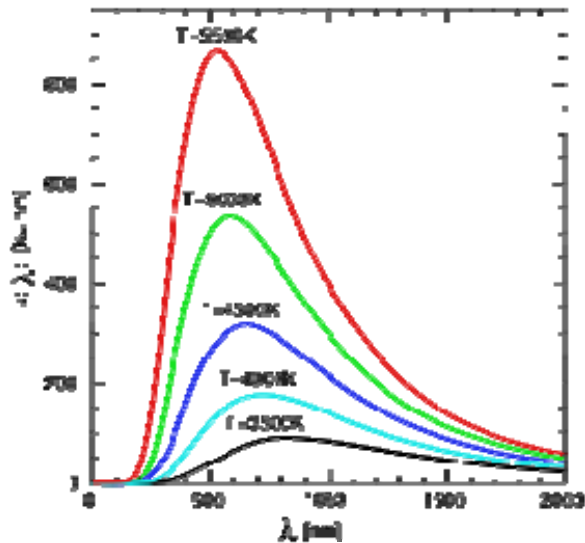


**Figure 2-1: Specific energy versus wavelength at different temperatures for the electromagnetic radiation emitted from a black body.**

As the temperature increases, the peak intensity shifts to higher energy, smaller wavelength radiation. The total energy emitted by a black body is found by calculating the total area under the curve and is a function to the fourth power of the absolute temperature as given by Stefan-Boltzman Law:

$$E = \sigma T^4 \tag{2}$$

19

From the above, it is inferred that all bodies emit and absorb Infra-Red (IR) radiation with varying intensities depending on the their temperature. A technique that takes advantage of this phenomenon is IR-thermography, which measures the intensity of IR radiation coming from a body and translates it to temperature.

Unlike fluorescence techniques, IR-thermography does not require a source for illuminating or exciting the sample, but rather only collects the radiation coming directly from the sample as a natural result of being above absolute zero. IR-thermography has the major advantage over other temperature measurement techniques in that it is non-invasive. Also, data collection is quite rapid. Another advantage of IR-thermography is that the solid temperature is measured and not the gas phase temperature. IR-thermography has been employed in a wide range of applications, ranging from high-end composite stress and fracture analysis, to high-speed screening in combinatorial chemistry [51, 52].

Although IR thermography using an IR-camera cannot be used to resolve temperatures within an individual channel, the ability to measure temperatures over a surface makes it useful in studying temperature effects of fast reactions with axial gradients. Therefore, a typical setup of a flow reactor where IR-thermography is used consists of an IR transparent material enclosing the region under investigation, which in many cases is the reactor's body. As a result, IR-thermography has so far been used for monitoring temperature gradients in 'open channels' or over the surface of a PBR or a monolith body.

The first use of IR-thermography as a technique for spatially resolving the reaction temperatures across the surface of a catalyst was employed by Schmitz et al. [29] who studied the temperature formation patterns during $H_2$ oxidation over a $Pt/Al_2O_3$ wafer resembling a CSTR. The motivation for their work was the inference that since catalyst particles on the atomic scale are inherently not the same in terms of active site geometry,

and hence activity, it would be logical to assume that the functioning of those particles on the macroscopic scale would also lead to variation in activity over the wafer itself.

Indeed, different catalyst concentrations led to different patterns observed, and although in some cases they presented evidence of non-uniformity, they attributed all pattern irregularity to non-uniformity rather than including explanations derived from heat and mass transfer contributions as well.

Luss et al. [30-34] conducted a series of experiments using IR imaging to observe temperature and hot zone patterns on radial and packed bed reactors. The first study was aimed at monitoring ignition and extinction reaction fronts formed during the oxidation of $NH_3$ over an electrically heated Pt ribbon [30]. They were able to resolve very slow reaction front motion, which was otherwise indistinguishable from stationary fronts, thus supporting the theoretical prediction of a single value of electrical current at which the velocity of the reaction front became zero.

Following that, they observed the dynamics and formation of hot zones in a radial flow reactor during CO oxidation over a $Pd/Al_2O_3$ catalytic reactor [31]. Hot zones were observed and started to form in a number of patterns close to the extinction point from the fully ignited state. They suggested that an accurate mathematical formulation of the problem must take into account the interaction of reactant diffusion rate, axial heat dispersion, rate of heat generation, changes in fluid properties, and inherent non-uniformities within the catalyst. They concluded that simple convective heat and mass transfer properties used for wrong way behavior representation are inadequate.

In another study, Luss and coworkers also used IR thermography to study hot zone formation during CO oxidation over a shallow packed bed containing several layers of spherical 0.3 wt% $Pd/Al_2O_3$ catalyst pellets (3-4 mm) [32]. They observed the formation of transversal hot zones close to the extinction point after cooling down from a fully ignited state. No explanation was offered for the patterns seen, but rather they offered a list of physical phenomena that might have been present and contributed to the existence

of such complex patterns, such as heat and mass diffusion rates, reaction rates and non-uniform activity. Overall, it was suspected that the chaotic behavior of the hot zone near the extinction point could have been avoided by operating at a lower flow rate. The variable in this study was the number of layers of catalyst pellets (i.e. bed depth). Space velocity was varied by increasing the bed depth by adding extra layers of catalyst; however, the workers attributed the non-uniformity of the active phase distribution to the hot zone pattern formation. A better way of analyzing the effect of varying space velocity on the hot zones formation would have been to vary the flow rate, instead of adding more of the catalyst whose uniformity was not well controlled.

In another study on shallow PBRs, they studied hot zone formation during the hydrogenation of ethylene and acetylene mixtures [33]. The reason for studying a different reaction was the expectation of different hot zone patterns. Another objective was to find the range of feed composition and temperatures that would lead to hot zone formation. Indeed, stationary non-uniform hot zones were observed. For some feed conditions, oscillatory non-uniform hot zones were observed as well; however, such conditions were different from industrial operation of PBRs for this reaction. The reason for the existence of the stationary non-uniform hot zone was attributed to non-uniformity in the PBR activity.

In one of their latest studies regarding hot zone formation [34], they suggested that reaction kinetics have a larger impact on hot zone formation induction than transport processes. To prove their claim, they ran experiments with identical conditions, but with different reactants that have different oscillatory reaction rates, namely $C_3H_6$ and CO oxidation. They concluded that due to the difference in the period of motion of the hot zone in shallow PBRs, the formation of hot zones is governed by the kinetics and adsorption strength of the reactant, and not by the thermal or flow properties of the reactor.

Wolf et al. [35-37] also utilized IR thermography to study spatial temperature patterns and hot zone formation for catalyzed reactions. In one study they used IR thermography

to observe the spatiotemporal temperature patterns and hot zone formation during CO and $C_2H_4$ oxidation over a 5% $Rh/SiO_2$ catalyst [35]. They attempted to relate the microstructure of the active phase, and the segregation or "communication" of the active phase, to the behavior of the temperature waves observed in an oscillatory regime. They used in-situ IR spectroscopy to evaluate the bonding structures of CO during oscillations, but were unable to find a relationship between the state of the CO-active site bond and the macroscopic oscillatory patterns. They attributed the slower hot zone motion from one active region to another on the same inlet wafer, as well as the higher localized heat, to an increased crystallite size that was deliberately induced during preparation.

In another study they evaluated CO oxidation over three catalysts; 0.4% $Rh/SiO_2$-Al, a CAMET metallic catalytic converter, and 1% $Pt/Al_2O_3$ [36]. The most interesting finding in the study was the absence of an oscillatory regime on the CAMET converter. According to the authors, the metallic substrate of the converter was disqualified as a probable cause, since the $Rh/SiO_2$-Al catalyst on which oscillations were observed, had a similar metallic aluminum base. The occurrence of an oscillatory reaction regime was attributed to the non-uniformity of the active phase dispersion on the wafer as compared to the monolith.

In a following paper [37], they extended the study discussed above to evaluate the possibility of suppressing the oscillations by perturbing the feed. Oscillations as related to conversion meant lower $CO_2$ formation during the extinguished low temperature state, and higher $CO_2$ formation during the ignited higher temperature state, a process which kept on recurring in the oscillatory regime. They concluded that by appropriately perturbing the feed they were able to lower the CO coverage and suppress the oscillatory behavior, hence maintaining the steady state at a lower overall catalyst temperature.

## 2.4 Spatially Resolved Capillary Inlet Mass Spectrometry (SpaciMS)

So far, no technique has proven viable in performing intra-channel gas phase speciation without direct invasive sampling. NMR holds promise, but is still in its infancy for wide application on various reactor configurations. The degree of interference and speed of sampling and response, however, differs widely from one technique to another. A technique that has proven highly successful in enabling spatio-temporal concentration measurements with minimal invasiveness and high sampling rates is SpaciMS, which has been developed in the Fuels, Engines and Emissions Research Center at Oak Ridge National Laboratory [38-40].

Partridge et al. [14] employed SpaciMS to study the NOx storage and regeneration efficiency of a $Pt/K/Al_2O_3$ monolith catalyst using spatial reactant and product concentrations and breakthrough profiles (as was shown in a previous section). In summary, they found that $O_2$ was quickly removed from the gas phase during a short regeneration step of 4 seconds by reaction with CO, which only occurred at the front end of the monolith. This CO oxidation caused an increase in the monolith's body temperature increasing the regeneration step temperature [41]. Further to what was discussed above, in S-exposure studies, they observed that sulfur deposition reduced NOx reduction but maintained NO oxidation and oxygen storage reduction capabilities. Also, full performance was restored after removal of sulfur at high temperatures. In a recent study [42] they showed that three primary zones existed within an NSR; a sulfated zone, an NSR zone and an OSC-only zone, and that the axial distribution of those zones was affected by temperature and sulfur loading.

Schmidt and co-workers have used such a technique for resolving species concentrations [43]. In an early study, they characterized methane catalytic partial oxidation (CPO) for the production of syngas in a millisecond foam catalytic reactor. Although several models were proposed for this reaction, there was still some debate about the mechanism. Mass

spectrometer data led to the conclusion that there were two reaction zones present; an initial oxidation zone in which CO was formed, followed by a reforming zone in which $H_2$ and CO were formed. $CO_2$ was formed in small amounts within the oxidation zone and remained constant throughout. No $CO_2$ reforming was observed except at a C/O ratio = 0.7 where $CO_2$ production was attributed to the WGS reaction. The size of those two zones was dependent on the carbon to oxygen ratio, as well as the total flow rate. They also performed numerical simulations that proved to be in agreement with the experimental results.

In a following study [44], CPO of n-octane for $H_2$ and olefin production where studied by monitoring the internal concentration and temperature profiles within the reactor. This time, the capillary was stationary along with a thermocouple at the very end of the bed, and the beds mass (height) was the variable. Also, the selectivity and productivity of syngas was compared between for different C/O ratios, flow rates, and between Pt- and Rh-based catalysts. Again, two zones where observed. In the upstream zone, oxidation of the octane into smaller hydrocarbons, $H_2O$, $CO_2$, $H_2$ and CO occurred. The second zone was larger and the smaller hydrocarbons reacted with $H_2O$ and $CO_2$ via reforming to form more syngas.

Those two studies showed the success of SpaciMS to resolve concentration profiles in fast reactions that have strong gradients along the reactor.

# CHAPTER 3: Experimental Set-Up and Procedure

## 3.1   The Catalyst

The catalyst used was 1% $Pt/Al_2O_3$ supported on a cordierite monolith supplied by DCL Inc. The cell density was 64 channels/cm$^2$. A 3"×3" square sample was cut to fit into the reactor. The sample had 120 channels divided equally between two rows. Figure 3-1 shows a schematic of the sample's geometry, but for a three cell deep sample.
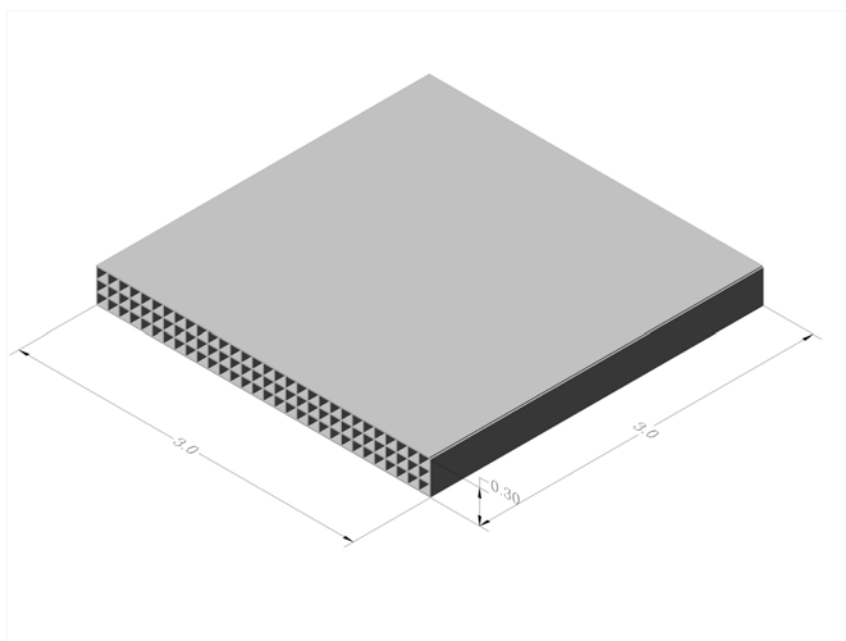


**Figure 3-1: Schematic of catalyst sample used inside the reactor.**

## 3.2   The Reactor

The reactor itself, with a schematic of its layout shown in Figure 3-2, is a stainless steel block divided into top and bottom sections along its horizontal axis. The sample is inside the reactor and is sandwiched between the two parts. To ensure a tight seal between the

top and bottom steel housing sections of the reactor, a diamond shaped groove is cut in the reactor's bottom section. A heat-expanding insulation material supplied by 3M is placed inside the groove, so that the reactor seals when heated the first time. The gases enter through a 0.25" ID tube in the bottom. The gases then enter a chamber that is tapered from the 0.25" hole to a 3" wide space, to minimize gas flow turbulence at the catalyst. The same chamber shape is used at the outlet side. The top section has a 3" by 3" square opening cut into its center, the same dimensions as the catalyst. When the catalyst is placed inside the reactor, one surface was completely exposed to this top opening. A third reactor piece, here called the cover plate, is used to seal this top cut-out of the reactor. The cover plate also has the square opening and is centered over the one in the top reactor section. The cover plate sits on top of a sapphire window that sits on top of the top reactor section, thus the sapphire window acts as the upper seal. The sapphire window has a diameter of 4.75". Again, the heat-expanding insulation is wrapped around the circumference of the sapphire window to prevent gas leaking around the sides of the window. Between the cover plate and the window, some of this matting material is also used to guard the window against scratching and breaking, but this also allows the cover plate to be bolted to the top half of the reactor housing to give extra pressure on the window to make a better seal.

With the window sitting on the cover plate, a clearance of 0.09" exists between the surface of the catalyst and the bottom of the window, forming a conduit for gas flow over the catalyst surface.

Four holes were drilled into the top reactor section, into which four thermocouples were inserted. One was used to measure the temperature of the inlet gas stream; one was inserted 0.5" into a monolith channel, one channel away from the center channel in the top row. The third thermocouple was placed into the center of the monolith (1.5" from the inlet) through a channel, two channels away from the center channel. The fourth thermocouple was placed 1" from the inlet, into a channel that is one channel away from the center channel.

The entire reactor is enclosed in a custom designed furnace, manufactured by Watlow. The upper portion of the furnace also has a square opening with dimensions matching the opening in the top section of the reactor and the catalyst sample. The depth of the aperture through the furnace is 5", being large to minimize heat losses. With this configuration the IR camera has an unobstructed view of the surface of the catalyst. Figure 3-2 shows a top and profile views of the reactor.
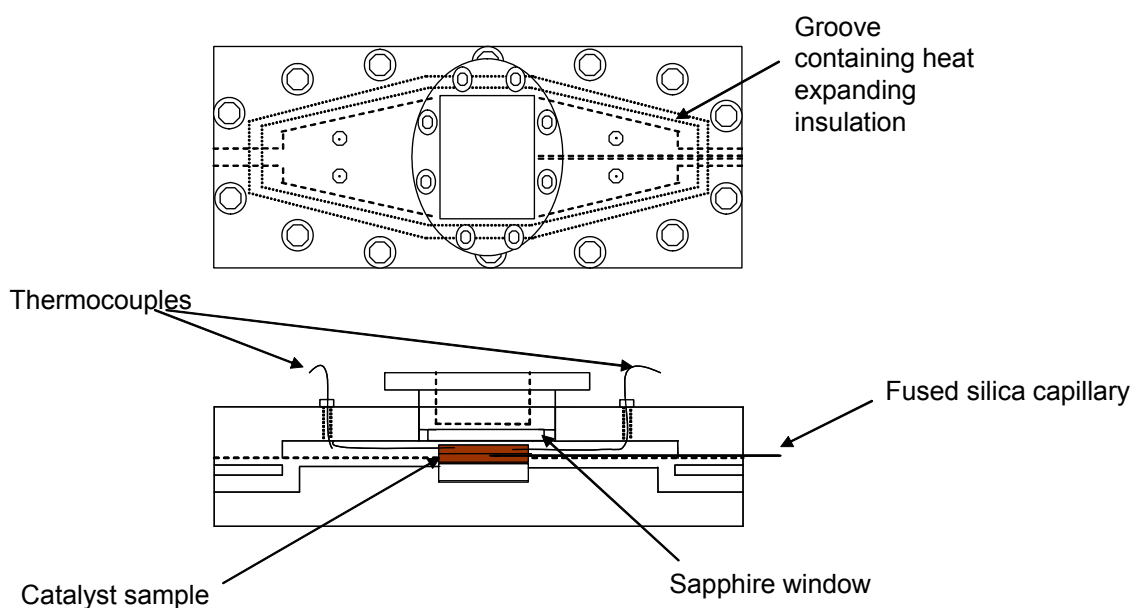


**Figure 3-2: Top and profile view of the reactor and catalyst sample configuration.**

## 3.3  Experimental Procedure and Process Schematic

Propylene and oxygen were fed to the reactor from compressed gas cylinders supplied by PraxAir. Also, for mass spectrometer calibration purposes, 50 mL of He were always flowing through with the reactants in the gas feed stream. The composition of the inlet gas stream was 0.5% $C_3H_6$, 6.5% $O_2$, 0.66% He and a balance of $N_2$. The $N_2$ was made using an On-Site nitrogen generator. Excess $O_2$ was added to ensure that $O_2$ would not be the limiting reactant. The gases were metered through Bronkhorst mass flow controllers. Before entering the reactor, the gases went through a preheating tube, preset

to a specified temperature. The gas stream leaving the reactor then went through an MKS 2030 FTIR analyzer, after which it was vented to exhaust. Figure 3-3 below shows a process schematic.
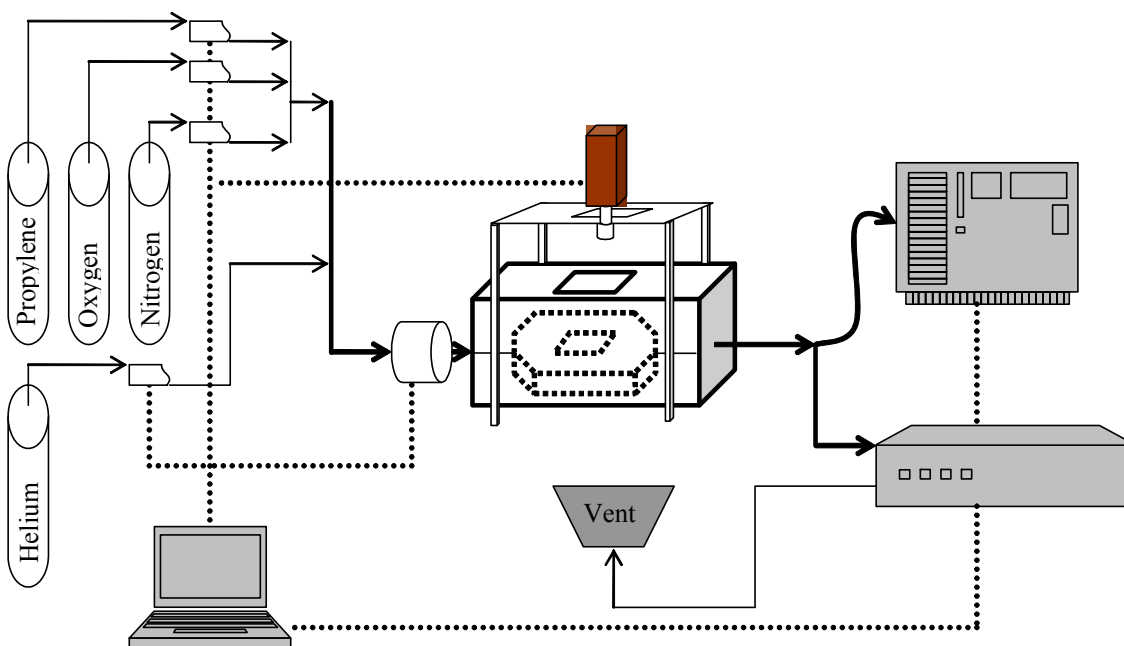


**Figure 3-3: Process flowsheet showing the flow of reactants and products through the experimental setup.**

In order to place a capillary at different locations in the catalyst, a groove was cut into the outlet side of the bottom reactor plate, extending from the outlet tube to the edge of the outlet side of the catalyst chamber previously shown in Figure 3-2. This groove housed the capillary which extended from one of the monolith channels to the outside of the reactor. It was sealed into the reactor via a septum. The capillary was fused silica with a 0.3 mm ID and a 0.43 mm OD. The end of the capillary coming out of the reactor was joined via a zero dead volume steel union fitting to the sampling end of a 6' capillary coming from a Hiden Analytical HPR 20 QIC mass spectrometer. The 6' capillary resided in a heated sheath and the capillary coming out of the reactor and the junction between the two capillaries was well insulated. The concentration profiles of $C_3H_6$, $O_2$, $CO_2$, $H_2O$ and He were monitored at 0.5" intervals from the inlet of the monolith.

For the mass spectrometer data processing, the correct percentage composition values of the monitored product and reactant gases were calculated by dividing the recorded partial pressure readings from the MS by the partial pressure of He (which was at a known fixed amount), and then applying a pre-defined calibration for each specific gas. This calibration of actual percentage versus measured percentage was found to be linear but different for all the gases within the monitored range of concentrations. A sample calculation is shown in Appendix A.

As mentioned earlier, a sapphire window was used since it is transparent to electromagnetic radiation in the 0.17-5 μm wavelength range. An IR camera, Merlin Mid InSb MWIR (Mid-Wave Infra Red), was mounted vertically on a stand and looked downwards on the surface of the catalyst through the sapphire window. IR cameras operate by measuring energy coming from the surface in the form of IR radiation, and the intensity of this radiation is related to the degree of 'hotness' of the surface. The camera used had a focal plane array consisting of a $320 \times 256$ 'starring' array of detectors, and is sensitive to mid wave IR radiation in the 1 μm to 5.4 μm range. The spatial resolving power of the IR camera is 0.012" (0.3 mm). The energy data collected by the camera were then converted to temperature using ThermaCAM Researcher software made by FLIR Systems Inc., which also controlled and operated the camera. An IR image of the catalyst surface as seen by the camera is shown in Figure 3-4.
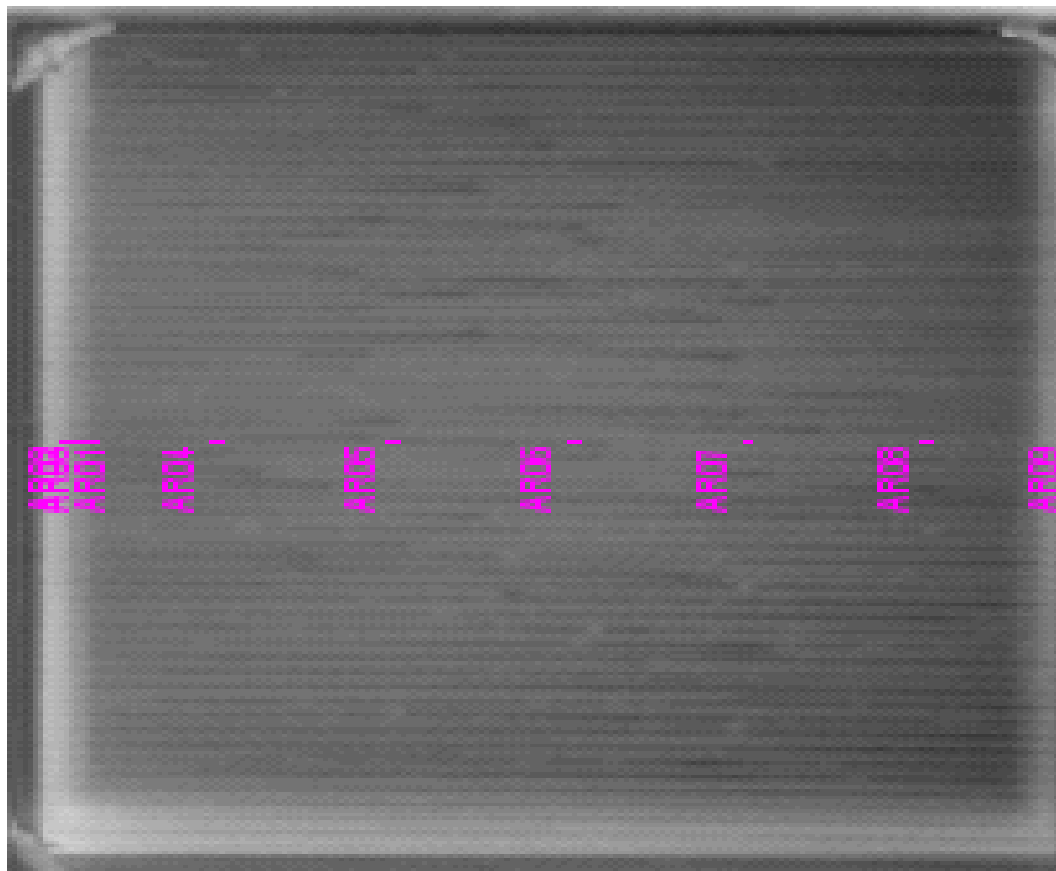
**Figure 3-4: IR image of the monolith surface as seen by the IR-camera. The nine positions at which the temperatures were monitored are shown.**

The data are stored as a sequence of frames that make up a movie file. Each frame is an IR image comprised of a matrix of temperature values that were 320 points in length and 256 points in width, i.e. matching the focal plane array. The catalyst itself filled 246 points in length and width. For our experiments, recording was done at a rate of 10 frames per second. Extracting the data from the movie files was done after the experiment was over.

Over 60,000 temperature data points per frame can be obtained from the catalyst surface. For presentation purposes, the data were extracted along a line taken at the center of the catalyst, parallel to the flow direction. This approach assumes no temperature gradients perpendicular to the flow direction. This assumption is reasonable for a highly exothermic reaction, and for uniform flow. Analysis of the data in the absence of reaction

indicates that the channels closer to the reactor wall are slightly hotter, by 3-5°C, during a temperature ramp. On the center line parallel with flow, 9 points were chosen for analysis and presentation. In Figure 3-4 above, a typical IR image of the monolith's surface and the position of 9 area points are shown. The reason for choosing those 9 locations downstream will become apparent in the results and discussion section.

There were two types of oxidation experiments; ignition and extinction. In an ignition oxidation experiment, the reactor temperature was ramped upwards and when the inlet gas temperature, as measured by the upstream thermocouple, reached 90°C, the camera, mass spectrometer and FTIR recording were started. When the inlet gas temperature reached 100°C, $C_3H_6$ and $O_2$ were introduced. A total gas flow of 7.6 L/min was used, which corresponded to a space velocity of 25000 $hr^{-1}$.

In an extinction experiment, the heaters were simply turned off at the end of the ignition experiment, and the reactants continued flowing. The reactor's temperature would eventually start to drop due to heat losses until complete extinction occurred, indicated by the outlet concentration re-achieving the inlet value.

Experiments were also done to determine the extent of heat conduction on the measured temperatures. The same gas stream compositions were used; however, instead of entering a cold reactor, the gas stream was adjusted to a steady inlet temperature of 313°C using the pre-heater and the reactor heater. This temperature was high enough to completely oxidize the entering $C_3H_6$ within the first 2.5% of the monolith's total length, similar to the steady state attained during the ignition experiments after complete $C_3H_6$ oxidation. These data therefore describe the temperature rise at any position downstream of the reaction zone that is due to heat conduction and convection transfer, which was then removed based on upstream temperatures.

The same experiments were repeated on a different sample, exposed to lab air in a closed furnace at 675°C.

## 3.4   CO Chemisorption Experiments

In order to determine the dispersion of the Pt particles before and after aging, CO pulsed chemisorption experiments were performed. Parts of the monolith were taken and crushed into powder with 48 Tyler equivalent mesh, with a cut-off of 300 μm particle size. 0.3017 g of powder was placed in a quartz tube which was set in a powder reactor hooked up to a Hiden Analytical HPR 20 QIC mass spectrometer.

For the chemisorption procedure, the sample was first heated in pure flowing He while increasing the temperature from 25 to 130°C at a rate of 10°C/min. Then the gas stream was switched to a stream of 5% $H_2$ in He and the temperature increased from 130 to 380°C at a rate of 10°C/min. The temperature was maintained at 380°C for 1 hr. The $H_2$ was then stopped and the sample treated in pure He (30 ml/min) for 10 min. The temperature was then reduced from 380 to 25°C in flowing He at 10°C/min. At 25°C, 100 μL of a stream of 5560 ppm CO in He was pulsed into the reactor at 60 second intervals.

The concentration of the outlet CO was constantly monitored using the mass spectrometer at the outlet. When consecutive CO pulses gave identical areas, within ± 1%, the experiment was stopped as the surface Pt sites were assumed to have reached saturation. The area under the curve of partial pressure vs. time for a pulse of CO at the end of this series, i.e. when none was sticking to the catalyst, was then correlated to the known inlet concentration. The area under the curves when adsorption was occurring was measured and hence the amount of CO adsorbed calculated, followed by the dispersion. The dispersions are reported in Table 3-1.

**Table 3-1: Dispersion values for fresh and aged powder samples.**

|  | Dispersion (Surface Pt/total Pt) |
|---|---|
| Fresh | **0.0382** |
| Aged at 675°C | **0.0211** |

As expected, the pulsed CO chemisorption experiments confirmed a reduction in dispersion after thermally aging the catalyst at 675ºC.

# CHAPTER 4: Results and Discussion

## 4.1 Proof of Concept

This section will illustrate how the temperature and concentration profiles were resolved along a monolithic catalyst during the propylene oxidation reaction.

### 4.1.1 Ignition and Extinction Experiments

Propylene oxidation was chosen because of its high exothermic heat of reaction, as well as its characteristic hysteresis behavior. The light-off temperature is defined here as the temperature at which the rate of reaction starts to instantly and rapidly increase. In most literature, only the outlet concentrations are monitored, therefore light-off has been commonly identified by a rapid increase in outlet conversion. The same is true for extinction, but with a rapid decrease in conversion instead. These two phenomena, ignition and extinction, occur when the inlet gas stream temperature reaches a certain temperature that is different in both cases; hence, a plot of outlet conversion versus inlet temperature resembles a closed loop, i.e. hysteresis. Figure 4-1 below shows a hysteresis plot of propylene conversion as measured by a downstream FTIR analyzer.
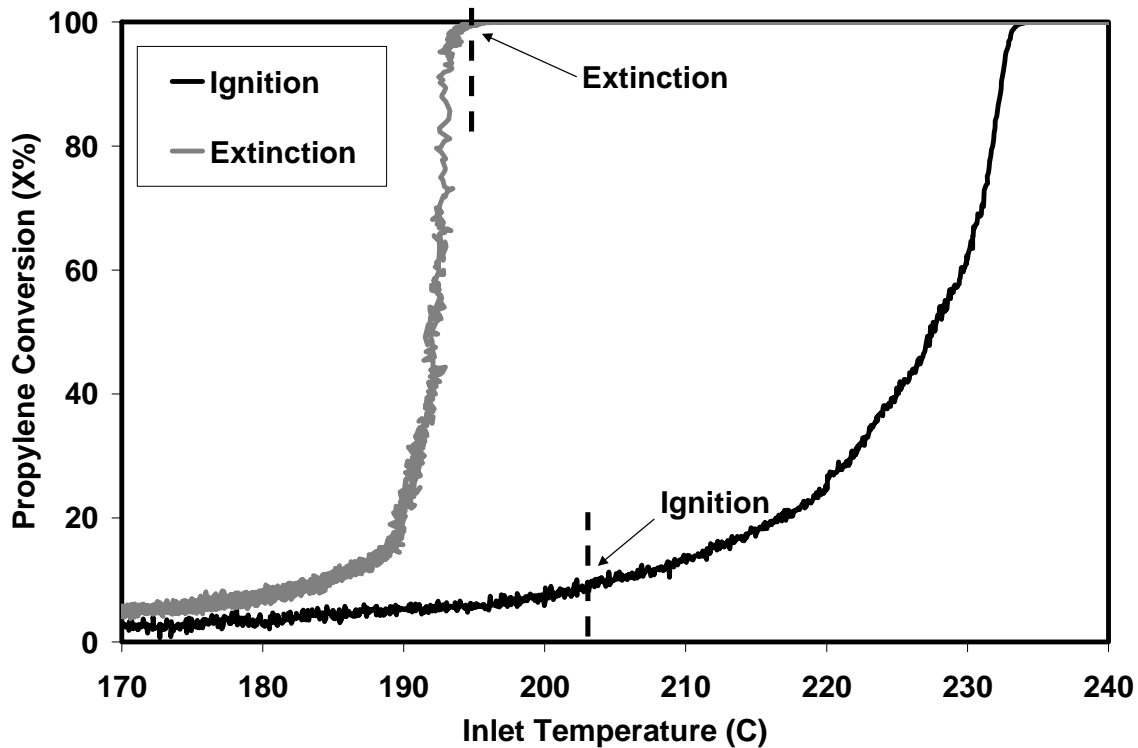
**Figure 4-1: Hysteresis plot of propylene conversion versus inlet gas temperature.**

Note the difference in ignition and extinction temperatures; light-off took place at an inlet temperature ~203°C, while extinction took place at ~194°C.

## *4.1.2 Wrong Way Behavior*

As has been mentioned above, and highlighted in the literature review, the dynamic patterns resulting from transient reactions in heterogeneous fixed bed reactors come in a number of forms. One such form arises close to the extinction point of an exothermic reaction, and is a transient phenomenon occurring in response to a drop in the inlet gas stream temperature, known as wrong way behavior. In essence, when the reaction is confined within a fixed reaction zone on the catalyst at steady-state, the rate at which the species travel to the reaction zone via a concentration wave, and at which heat is dispersed from this reaction zone via a temperature wave, are balanced. Due to the

thermal inertia of the ceramic monolith, any perturbation in the steady-state conditions such as a drop in the inlet gas stream temperature would upset this steady-state and would cause the temperature and concentration waves to travel at different speeds. When the inlet temperature decreases, the concentration wave travels with the convective flow at a much higher speed than the temperature wave. This causes a higher concentration of the un-reacted species to reach the reaction zone, reaction occurs and a spike in temperature, above the steady-state temperature established prior to the inlet temperature decrease, is observed. The effect of the decrease in inlet temperature on the temperature is slower due to the higher thermal inertia of the monolith body.  If the temperature continues decreasing, then this spike in temperature moves as well, generating a wave-like temperature profile that travels downstream until the catalyst outlet and extinction occurs [45].

In the experiments conducted, as indicated in the experimental description section, after complete ignition was observed, the heaters were turned off. The reaction at this stage was semi-self-sustaining, as it continued using the heat generated via the exotherm. Eventually, however, with the reactor cooling down because of heat losses to the surroundings, wrong-way behavior was observed close to the extinction point. Temperature profiles showing the wrong-way behavior are presented in Figure 4-2.
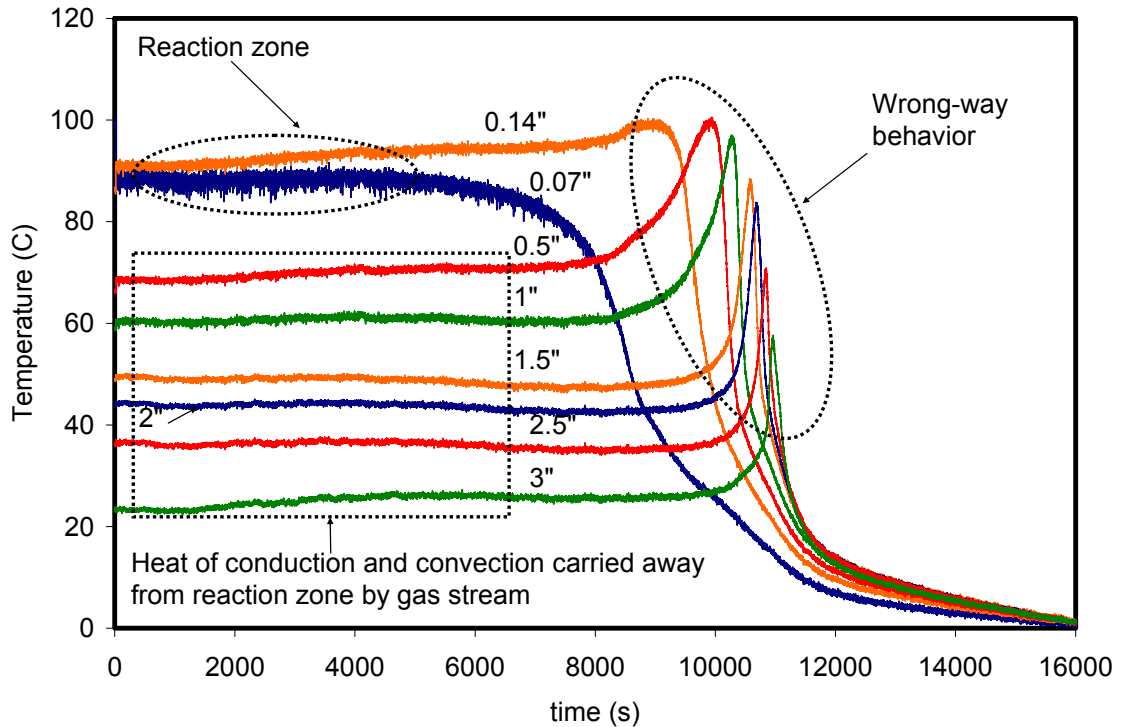
**Figure 4-2: Wave-like temperature profiles, characteristic of wrong-way behavior, over the surface of the monolith near the extinction point of the propylene oxidation reaction.**

It is apparent that the reaction zone was initially confined within the first 0.14" inches of the catalyst, indicated by the highest temperature rise of ~90°C at that position. The temperature rises seen at downstream positions were due to the heat of conduction through the monolith and heat of convection from the heated gas passing through the reaction zone.

## 4.1.3 Moving Hot Zones

With confidence that IR-Thermography was reliable in capturing the dynamic features of temperature changes as they developed over the surface of the catalyst, the exothermic propylene oxidation reaction was characterized during light-off. This led to evaluation of moving hot zones, discussed in the literature review section.

## 4.1.3.1   Temperature Ramps

As mentioned in the experimental section, "blank" temperature ramps, where no reactants were added, were conducted so that the background heat from the furnaces could be subtracted and the reaction heat effects isolated. Multiple ramps were done to ensure reproducibility. Figure 4-3 contains the temperature profiles as a function of time obtained at the nine positions during such a temperature ramp.
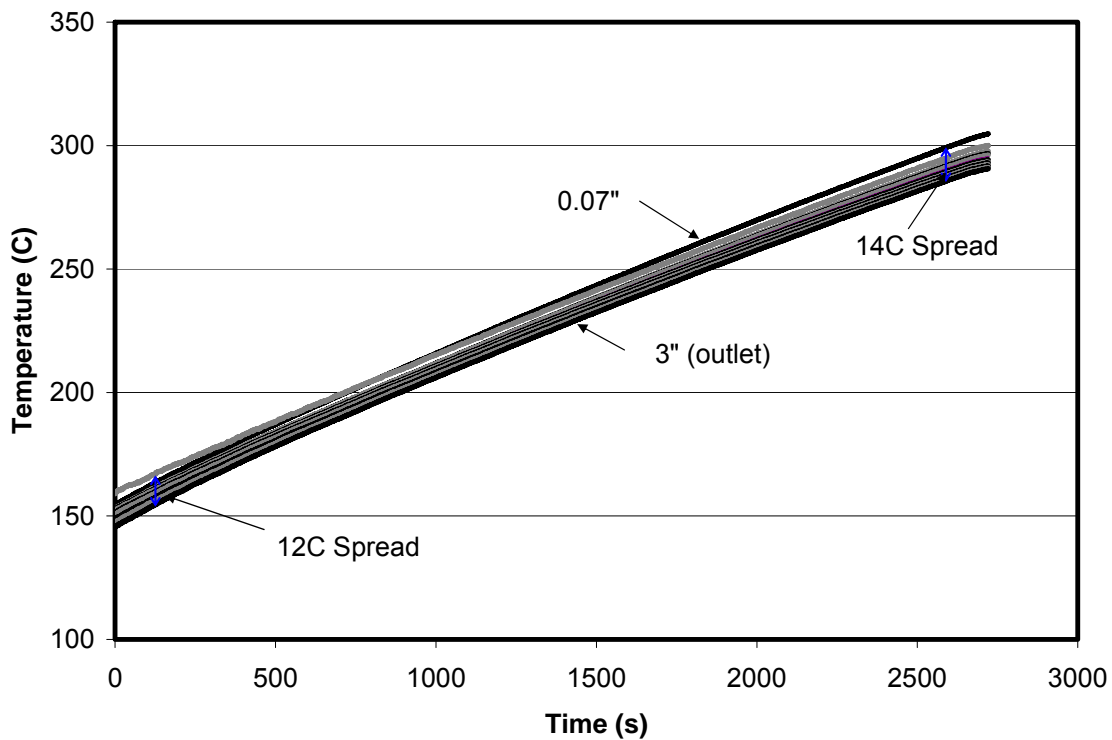


**Figure 4-3: Temperature profile at nine positions over the surface of the monolith during a temperature ramp with no reaction.**

From Figure 4-3, the maximum temperature difference between the position at 0.07" and the back of the monolith at 3" was 12°C. This difference in temperature is due to extra heat from the upstream pre-heater. This difference was the smallest possible during a ramp for two reasons.

1- The large thermal inertia of the reactor due to its large mass, slowing the ability to quickly respond to heater input.

2- The sapphire window was not covered with insulation, which of course results in heat loss from the gases, leading to cooler temperatures downstream.

As the ramp increased, this $\Delta T$ between front and back increased, but only by 2°C over a an overall 150°C increase in temperature.

In Figure 4-4 below, the temperature profiles from two temperature ramp experiments carried out four days apart are shown. The profiles are overlaid for four positions; 0.7", 0.5", 2", and 3". It is apparent that the temperature profiles line-up closely, therefore leading to the conclusion that the temperature ramps could be reproduced and could be subtracted from temperature data that included reaction, in order to isolate reaction effects.
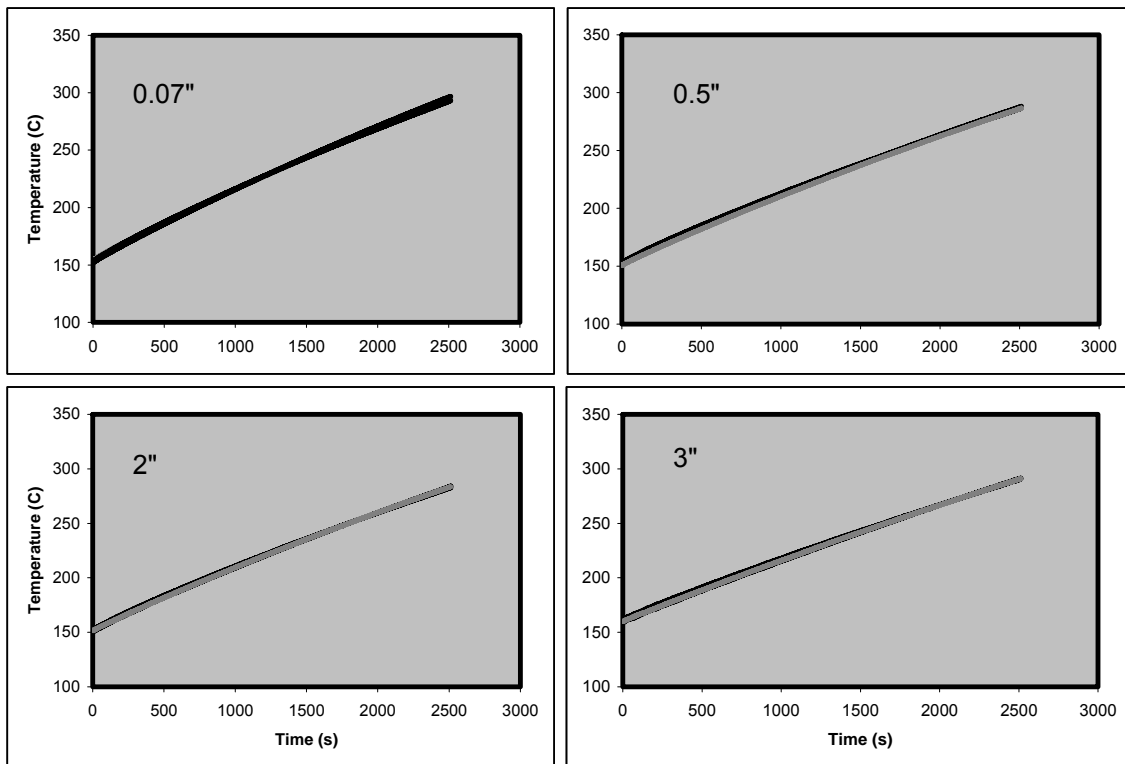


**Figure 4-4: Reproducibility of temperature ramps; temperature profiles for four positions from two independent temperature ramps.**

## 4.1.3.2 Un-aged (Fresh) Monolith Catalyst Sample

## 4.1.3.2.1 IR-Thermography Temperature Data

The temperature profiles as a function of time obtained during a propylene oxidation experiment at the nine positions are shown in Figure 4-5.
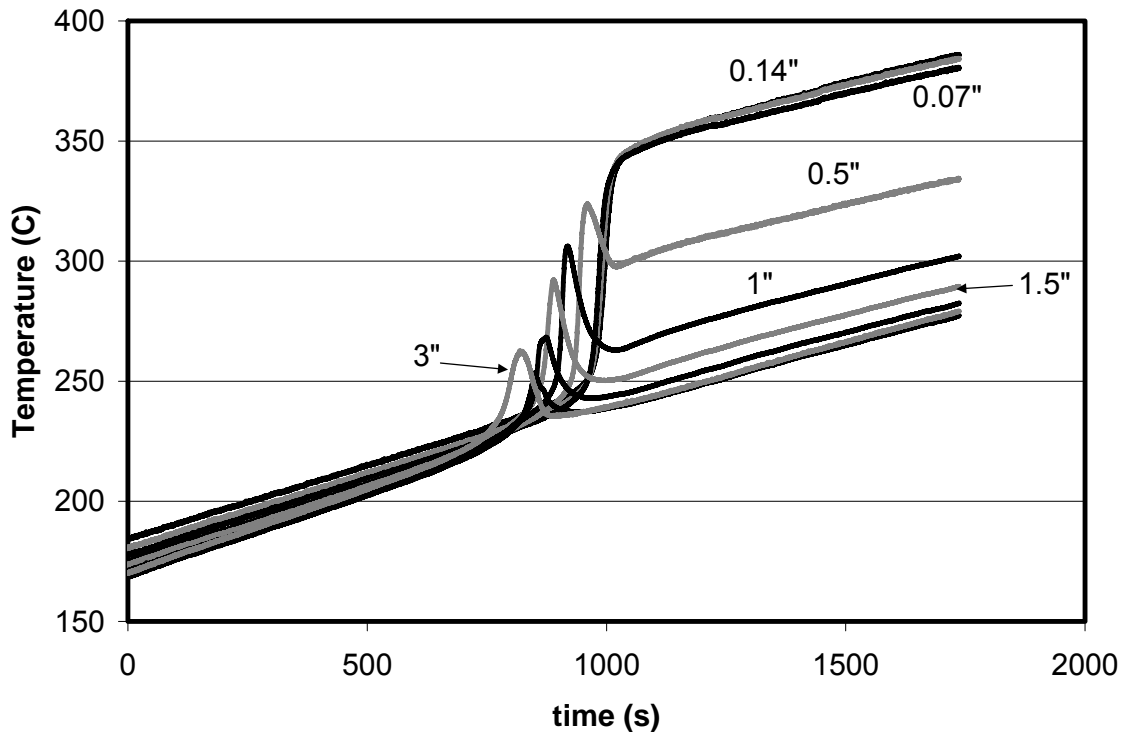


**Figure 4-5: Temperature profile at nine positions along the monolith surface during a ramped propylene oxidation experiment using the fresh catalyst.**

These data were obtained during a temperature ramp experiment as described previously. After approximately 750 seconds, an increased rate of temperature rise was observed at 3" from the inlet, or the most downstream position, peaking at 260°C before the temperature started to decrease at 830 seconds. After 900 seconds, the temperature again began to increase. After the peak in temperature was observed at the outlet position, the same trend was observed at every position upstream but at progressively later times,

41

giving a wave-like pattern that propagated against the direction of flow. Except at the 3 positions closest to the inlet, after a peak in temperature was achieved, the temperature dropped. This drop became smaller as a function of position, until at approximately 0.18" from the inlet, only a temperature rise was observed. The maximum temperature rise was observed at 0.14" from the inlet. These data in Figure 4-5 represent the first set of processed data obtained from the camera.

In order to better illustrate the temperature profiles due to the heat of reaction alone, the furnace contribution was removed by subtracting the baseline temperature profile of the heaters from the temperature profiles that included reaction. As was shown in Figure 4-4, multiple baseline measurements, obtained with no reactants entering, were taken to ensure that this subtraction could be done from experiment to experiment. The ramp was found to be linear and reproducible. Figure 4-6 depicts the concept of reference image subtraction, i.e. that of a no-reaction baseline subtraction. The representation shown in Figure 4-6 is for four positions.
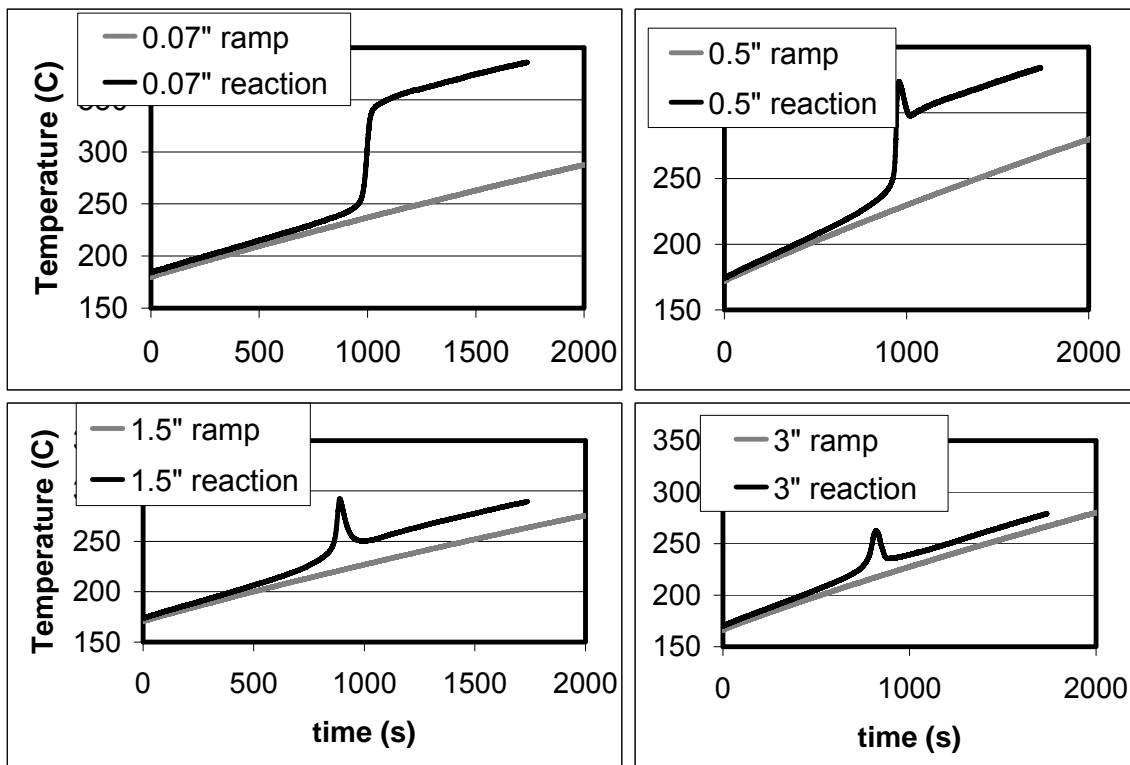
**Figure 4-6: Temperature profiles of a blank and a propylene oxidation temperature ramp overlaid on the same plot at four positions.**

The spatially-resolved temperature profiles as a function of time, with the temperature associated with just the heat ramp subtracted, are shown in Figure 4-7. These are therefore associated with heat release due to reaction alone, and the data are presented as differences in temperatures, i.e. $\Delta T$.
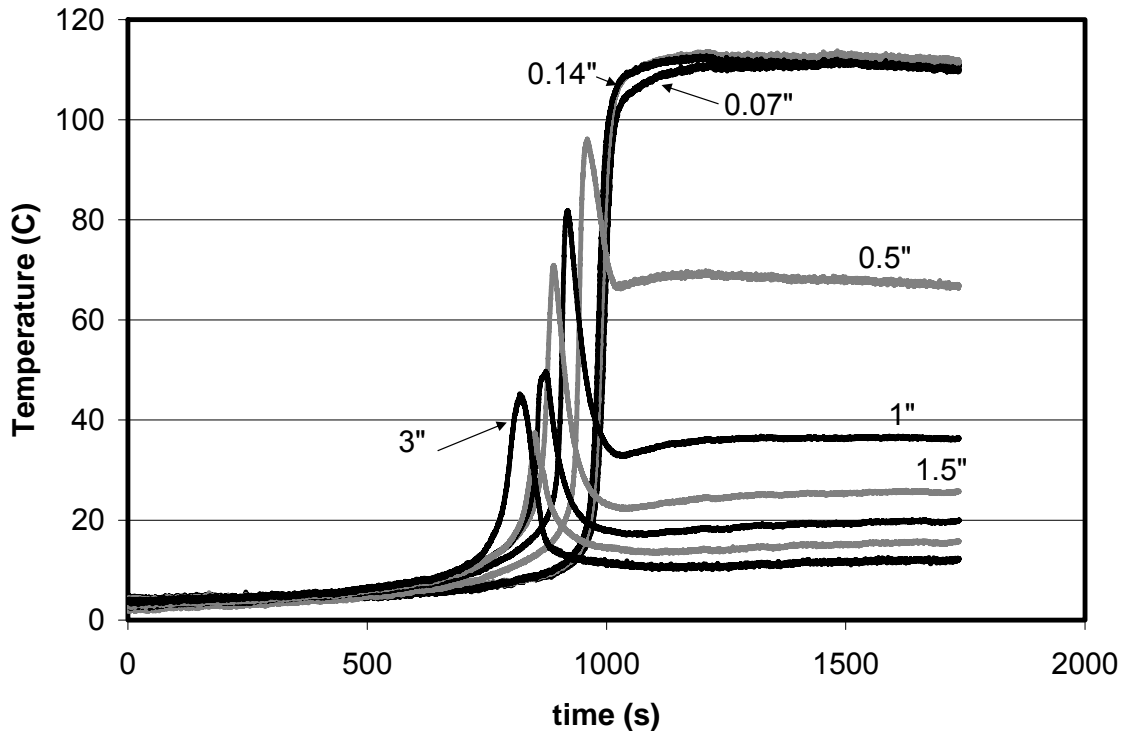
**Figure 4-7: Adjusted temperature profiles during a ramped propylene oxidation experiment with the heater contribution removed.**

At the most downstream position, where the first temperature rise due to reaction was observed, a maximum temperature rise of 40°C was observed. The maximum temperature change 2.5" from the catalyst inlet was smaller, 33°C, while all others increased as a function of catalyst position, until a maximum temperature rise of ≈111°C was attained at 0.14" from the inlet.

This moving temperature profile is a common phenomenon for exothermic and endothermic reactions in heterogeneous catalytic systems [16, 46]. The temperature profiles as a function of time seen in Figures 4-5 and 4-7 demonstrate that the reaction initiated, or ignited, at the rear of the sample and propagated toward the inlet until a steady-state was attained, with the reaction confined to a zone spanning the first ~0.18" of the sample. The width of this zone was verified by adjusting the position of the capillary, as will be discussed below, after the temperature ramp was ended. This

44

dynamic wave behavior from back (downstream) to front (upstream) was reported previously by Sheintuch et al. [20]. Also Jaree et al. [15, 47] demonstrated the upstream motion of a reaction front with increasing inlet gas temperature. Oh and Cavendish [18] predicted with their CO oxidation model that only a small section at the inlet of a monolith would be used for CO oxidation under certain conditions, i.e. the reaction zone was confined within a small region from the inlet at a high enough temperature.

These propylene oxidation experiments described were reproducible, as is shown in Figure 4-8 below, where the temperature profiles at four positions down the length of the catalyst from four different experiments are shown. The close match between the profiles visually indicates reproducibility.
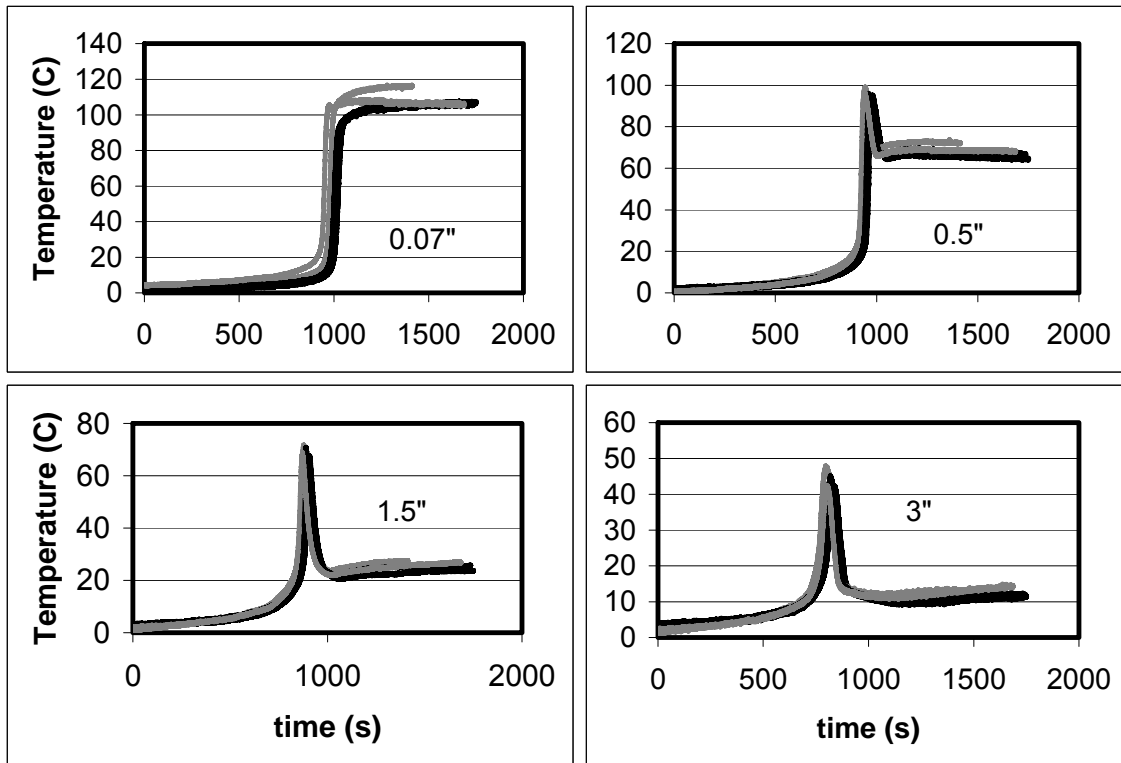


**Figure 4-8: Reproducibility check of data from ramped propylene experiments.**

## 4.1.3.2.2    Steady State Experiment Temperature Data

As will be proven from the SpaciMS data discussed below, the residual temperature rise after a peak had been achieved was due to heat transfer via conduction and convection downstream, from the high temperature reaction zone upstream. This point is highlighted in Figure 4-9 below.
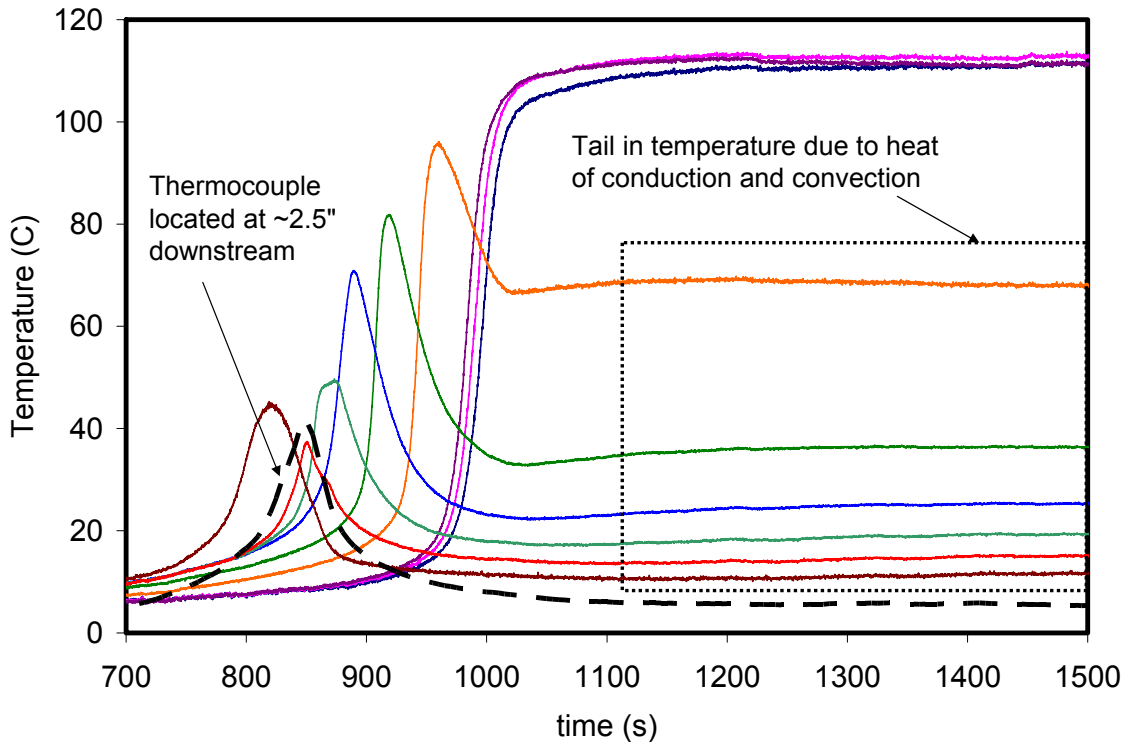


**Figure 4-9: Temperature profiles from nine positions during a ramped propylene oxidation experiment highlighting the temperature rise due to conduction and convection heat transfer only.**

The purpose of the steady-state experiments was to isolate the effects of heat transfer due to conduction and convection at positions downstream from the heat generated by the reaction. The data obtained from these experiments were then used to carry out a calibrated subtraction that would isolate reaction heat effects, enabling better analysis to be carried out.

46

The temperature profiles from a steady-state experiment are shown in Figure 4-10.
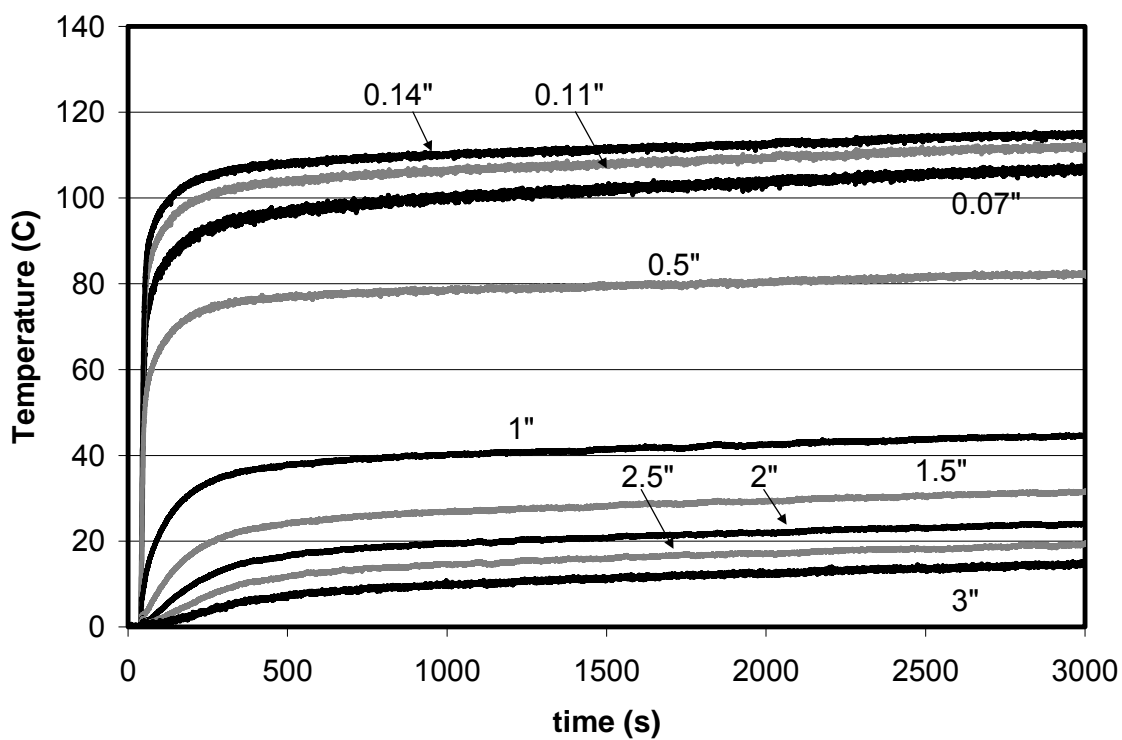


**Figure 4-10: Temperature profiles from nine positions during a steady-state propylene oxidation experiment.**

Propylene was introduced at ~220 seconds in the plot, and ignition occurred immediately at the catalyst inlet. The maximum temperature rise attained was identical to that observed during a temperature ramp experiment; see Figure 4-7, around 111°C. As will be proved later, the reaction zone was confined within the first 0.14" of the catalyst. A

47

drop in temperature rise of ~25°C is observed at 0.5" from the reaction zone, and is even greater at positions further downstream. The temperature rises attained at all positions downstream of 0.14" were solely due to heat carried away from the reaction via conduction and convection.

Reproducibility of the steady-state inlet temperature experiments was again tested, with the data shown in Figure 4-11. With the data reproducible, and the steady-state temperature rises matching those at the end of the temperature ramps, the conduction and convection heat transfer rates were also fixed for a given set of reaction conditions and the subtraction could be carried out with confidence, knowing that the adjusted temperature profiles would represent the heat of reaction.
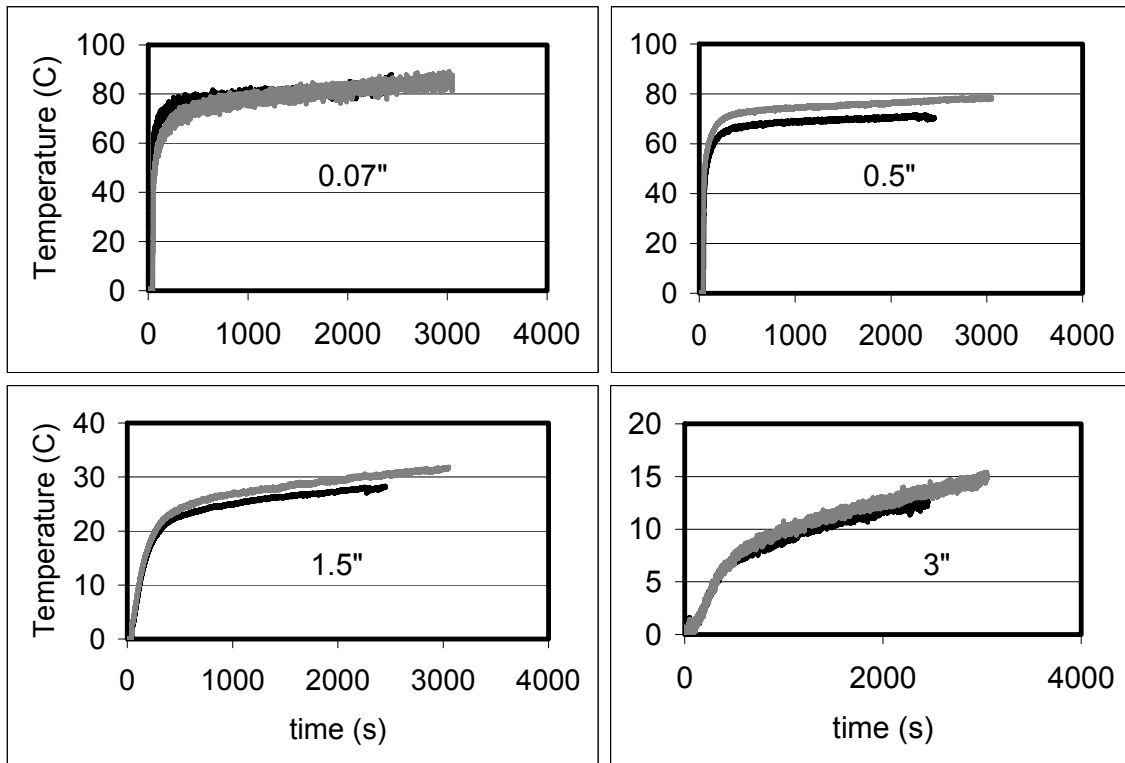


**Figure 4-11: Reproducibility of the steady-state propylene oxidation experiments, two experiments shown.**

In Figure 4-12, the conduction subtraction process is visually depicted for three positions.
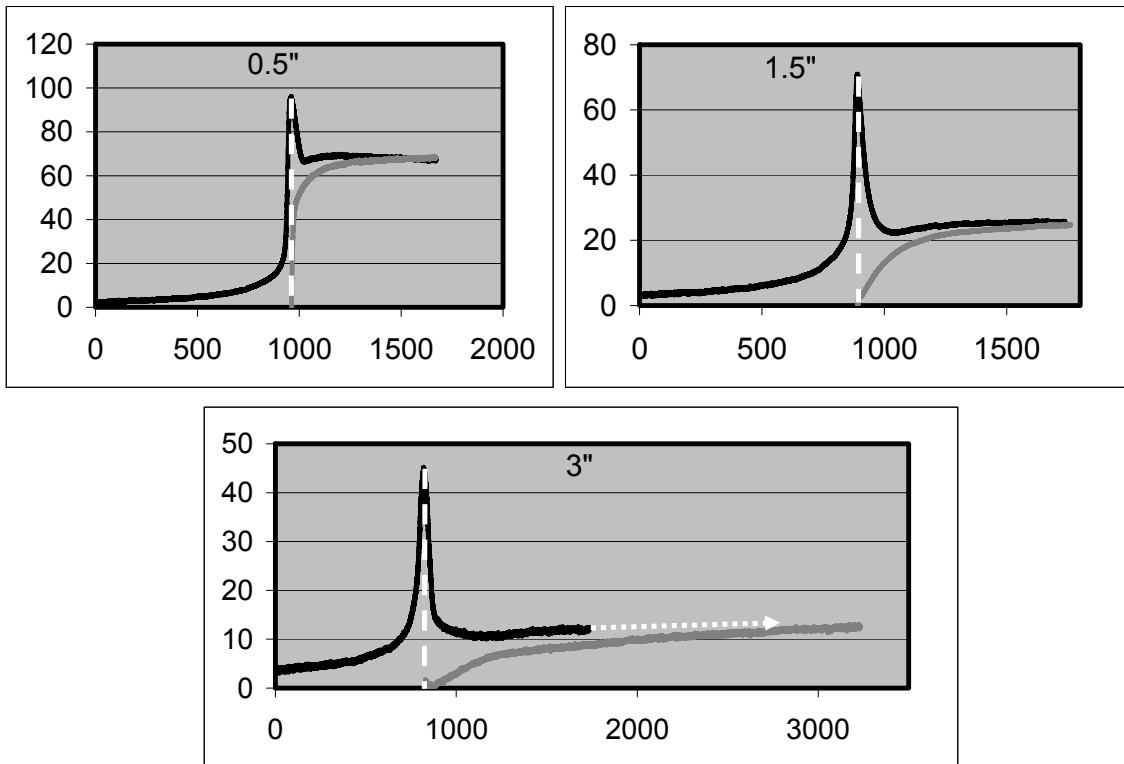


**Figure 4-12: Graphical depiction of the subtraction procedure for removing the heat of conduction and convection and isolating the heat of reaction.**

The subtraction of the conduction and convective contribution from the temperature ramp experiment data started at the point at which the temperature reached a peak during the ramp. The reason for this will be discussed in greater detail when discussing the mass spectrometer data.

The final spatio-temporal temperature data from the reaction heat generation is presented in Figure 4-13 below.
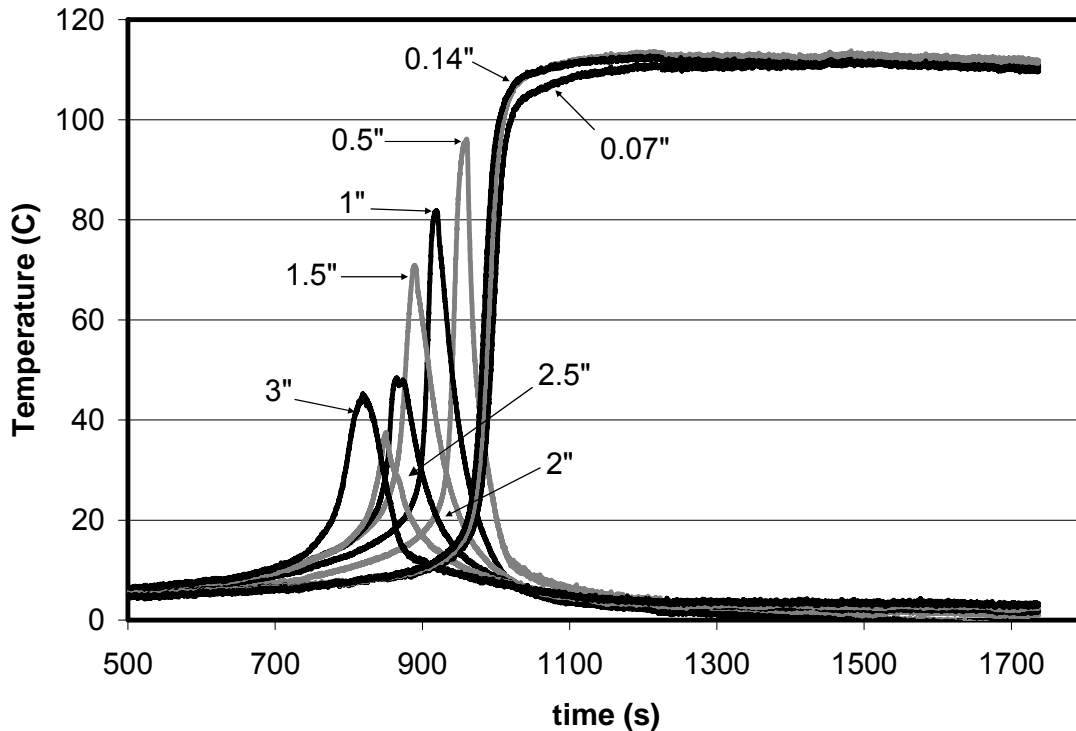
**Figure 4-13: Final, adjusted temperature profiles from nine positions obtained during a ramped propylene oxidation experiment after the heat associated with the furnace input and conduction and convection were subtracted. The temperature profiles are due to the heat of reaction only.**

## 4.1.3.2.3 Mass Spectrometer Concentration Data

As was discussed in the experimental section, the mass spectrometer data consisted of concentration measurements of the reactants, propylene and oxygen, the products, carbon dioxide and water, as well as the carrier and tracer gases, nitrogen, argon and helium.

The spatio-temporal concentration data were obtained by positioning the capillary at different locations down the length of the catalyst and repeating the same temperature ramp reaction experiment at every new position.

50

Also, as was indicated in the experimental section, the mass spectrometer recorded the partial pressures of the monitored species, and then a calibration, explained in Appendix A, was done on the data to convert the recorded partial pressures into concentrations.

In Figure 4-14, the spatio-temporal concentration profiles of the reactants and products after calibration of the MS data are shown. The data shown are from one propylene oxidation during a temperature ramp, with the capillary at 1.5" (center) in this experiment.
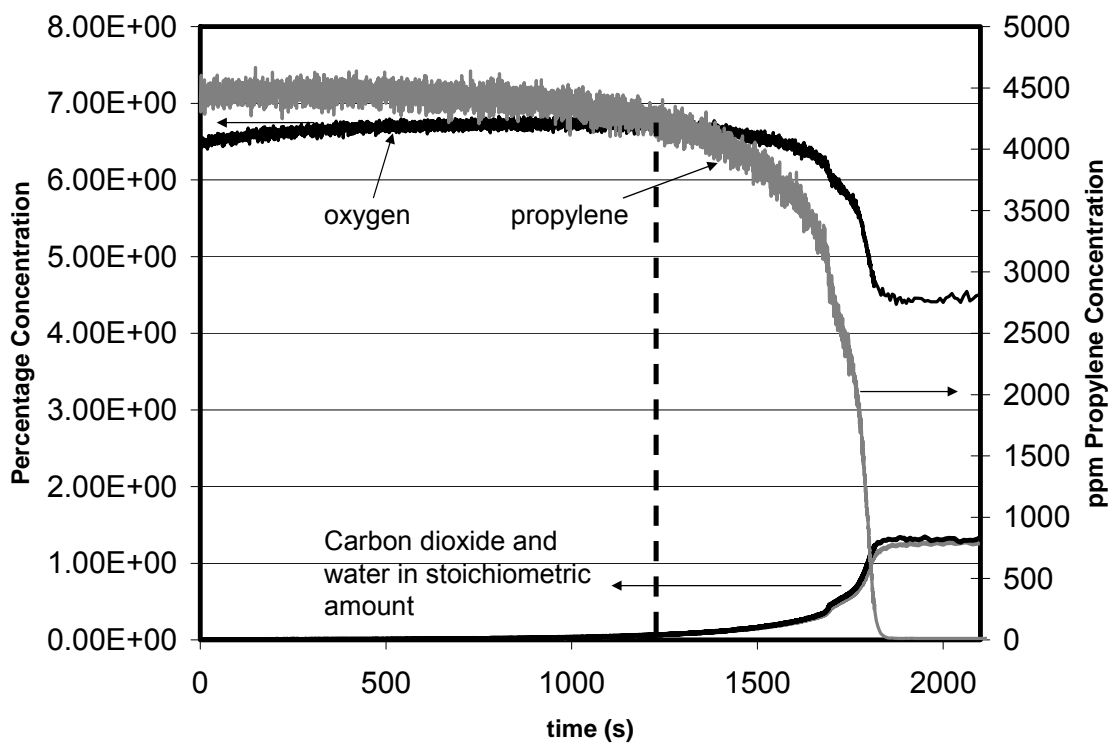


**Figure 4-14: Concentration profiles of reactant and product species after the calibration was applied to the data.**

In this experiment, propylene reacts completely within the sample, dropping from an inlet concentration of 0.45% to zero. Also, the oxygen, which was in excess, dropped from an initial value of 6.5% to 4.475%, i.e. 2.025% of the oxygen reacted. Finally both water and

carbon dioxide are produced in equal stoichiometric amounts and three times the molar concentration of propylene, following the $C_3H_6$ oxidation stoichiometry.

The data in Figure 4-14 indicate that the reaction was complete, and that the products were in stoichiometric proportions. Also, the products were first observed when the reactants concentration began to drop, at ~1230 s.

Based on the above, by inspecting the behavior of one species, the behavior of the remaining species could be deduced. Therefore, only the concentration of propylene will be shown in the following figures.

First, Figure 4-15 shows the reproducibility of the concentration data obtained using SpaciMS.
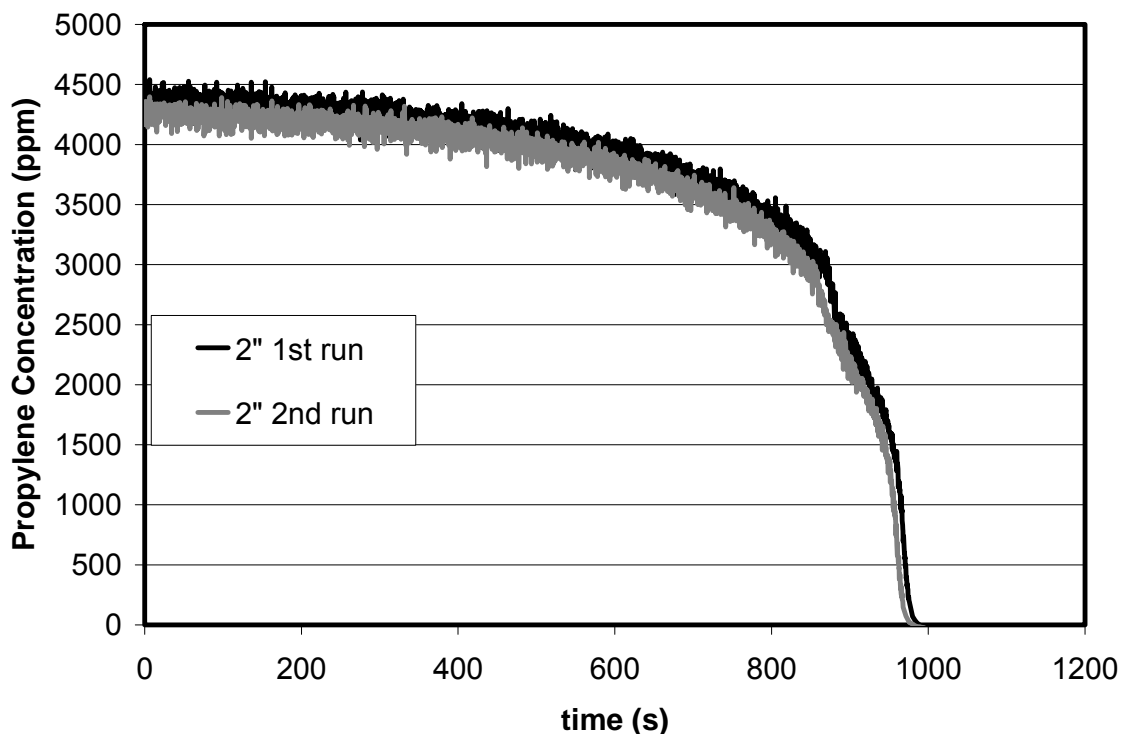


Figure 4-15: Propylene concentration profiles at 2" from two independent experiments.
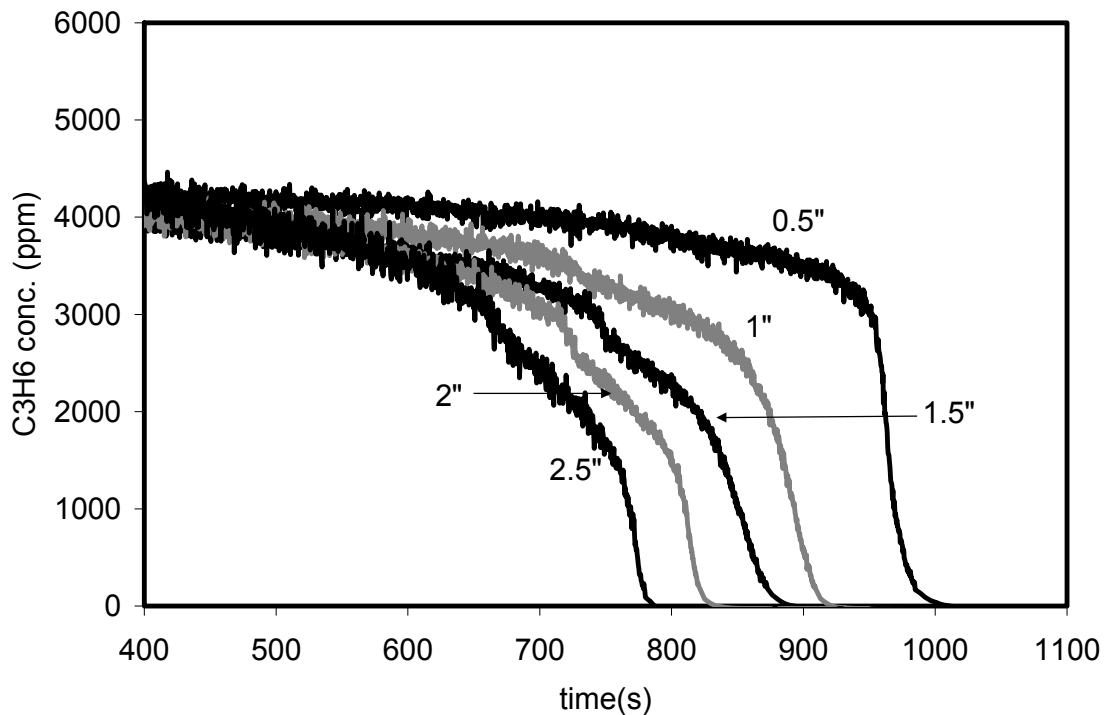
**Figure 4-16: Propylene concentration profiles at five equidistant positions along the monolith catalyst during a ramped propylene oxidation experiment.**

In Figure 4-16, the concentrations measured using the mass spectrometer at several positions are plotted. All the concentration profiles shown are lined up in time, with time = 0 seconds corresponding to an arbitrarily chosen inlet temperature of 176°C, which was lower than the light-off temperature. The propylene concentration at 2.5" from the inlet was decreasing from the start in this plot, but accelerated after t = 600 seconds. The slow decrease observed at early times, before 600 seconds, indicates some oxidation was occurring before what would typically be described as light-off. Similarly, some temperature increase was observed in Figure 4-7 prior to the rapid increase in temperature rise discussed above. The accelerated drop in concentration was observed at upstream positions at progressively later times. A drop to zero concentration at any position indicates the end of reaction at that point, with reaction then occurring at upstream positions.

From these data and the temperature propagation data in Figure 4-7, it is apparent that a reaction front evolved after light-off was observed at the catalyst outlet. This reaction zone moved upstream and based on the mass spectrometer data, no reaction was observed downstream of this reaction zone once it began moving upstream.

A comparison of the temperature and concentration profiles provides insight into the behavior of the reactant and product species as the reaction front moves upstream. In Figure 4-17, the temperature profile obtained at 0.5" from the inlet is overlaid with several concentration profiles, i.e. combining some of the data in Figures 4-7 and 4-16. The peak temperature rise at 0.5" from the inlet reached 94°C, and lined up exactly with the point at which the propylene concentration decreased to zero. The data are presented in a similar way in Figure 4-18, with the concentration profile at 1.5" from the inlet overlaid with several temperature profiles. The temperature at 1.5" from the inlet peaked at a temperature difference of 70°C, and lined-up exactly with the point at which the propylene concentration dropped to zero at that same position. The data presented in both Figures 4-17 and 4-18 indicate that no reaction took place after the temperature rise peaked and started decreasing.
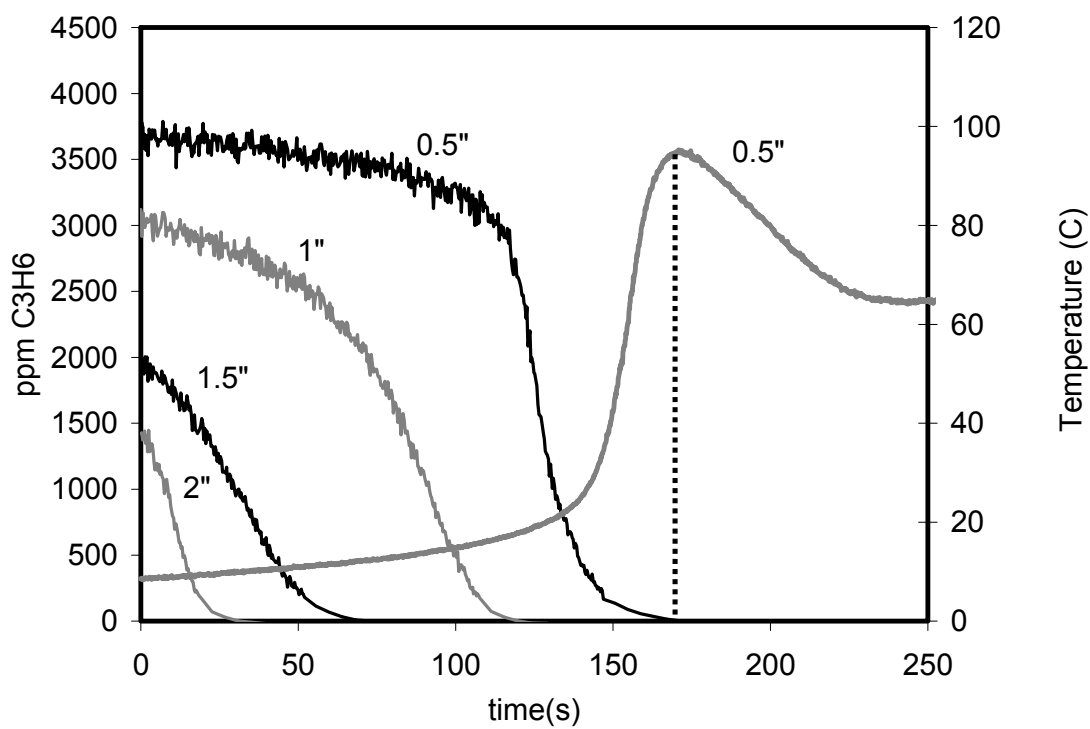
**Figure 4-17: Temperature profile at 0.5" overlaid on the same plot with four concentration profiles during a ramped propylene oxidation experiment.**
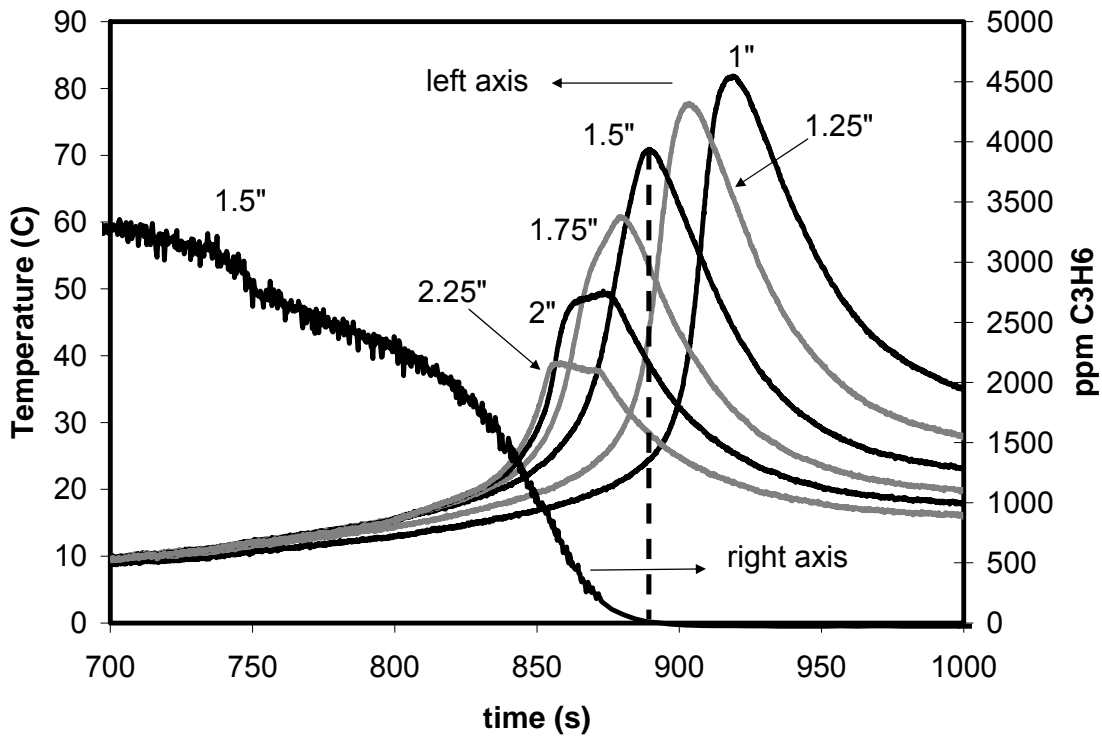
**Figure 4-18: Concentration profile at 1.5" overlaid on the same plot with temperature profiles during a ramped propylene oxidation experiment.**

The decrease in temperature difference after each peak at each position coincides with the mass spectrometer data demonstrating that the reaction front had passed that position. However, from just analyzing the IR thermography data, such a decrease would not conclusively show that no reaction continued to take place at that position. The temperature difference did not re-achieve zero, even after no reaction was occurring as confirmed by the concentration profiles. The temperature difference after the reaction is no longer occurring at that position is due to heat being transferred by conduction and convection down the monolith from upstream positions. For example, at 2" from the inlet, the temperature difference started decreasing after having reached its maximum at 81°C; however, the drop in temperature did not go to zero, but leveled off at 36°C. This steady-state temperature difference became larger at each upstream position. To account for the conduction effect, the calibrated subtraction described previously was performed. The re-processed data are shown in Figure 4-13, and with this subtraction it is apparent

56

that the temperature profiles now approach zero. In comparing these data to those in Figure 4-7, the decrease in temperature still coincides with the propylene concentration approaching zero, but the temperature difference drops rapidly, now clearly indicating that the reaction is no longer occurring to any significant extent at that position.

A plot of propylene concentration at different positions as a function of time is shown in Figure 4-19, with time at 0 seconds taken arbitrarily as the time when propylene concentration dropped to zero at the most downstream position, i.e. after light-off initiated at the rear.
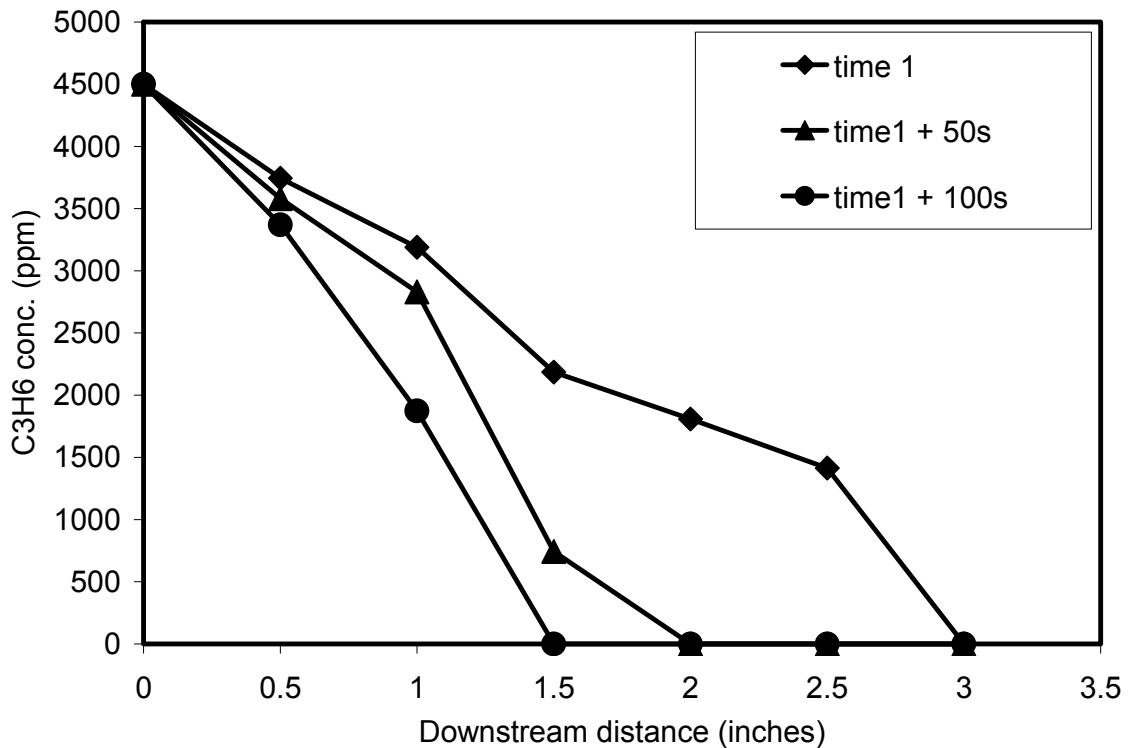


**Figure 4-19: Propylene concentration versus the distance downstream from the inlet (inches) as a function of time.**

As shown in Figure 4-19, at 0.5" from the inlet, the concentration dropped from 3745 ppm at 0 seconds, to 3370 ppm 100 seconds later. Further downstream, at 1", this decrease was more significant over the same time period, from 3188 ppm to 1873 ppm. At 1.5" from the inlet, the propylene concentration was at a lower value of 2185 ppm initially, but dropped to zero within the 100 second plotted time period, indicating that the reaction front had already passed that position after 100 seconds. This increase in the concentration differences highlights that after light-off, the reaction zone extended all the way from the inlet to what is sometimes described as, and what we are labeling, the reaction front, and is not just within a small portion of the catalyst. This reactive portion decreased in size as the front propagated upstream.

### 4.1.3.3  Aged Monolith Catalyst Sample

The data obtained by repeating the experiments described above, but with the sample aged at 675°C, are presented below.

### 4.1.3.3.1 Steady-State Experiment Temperature Data

The temperature profiles for a steady-state experiment for the catalyst aged at 675°C are shown in Figure 4-20.
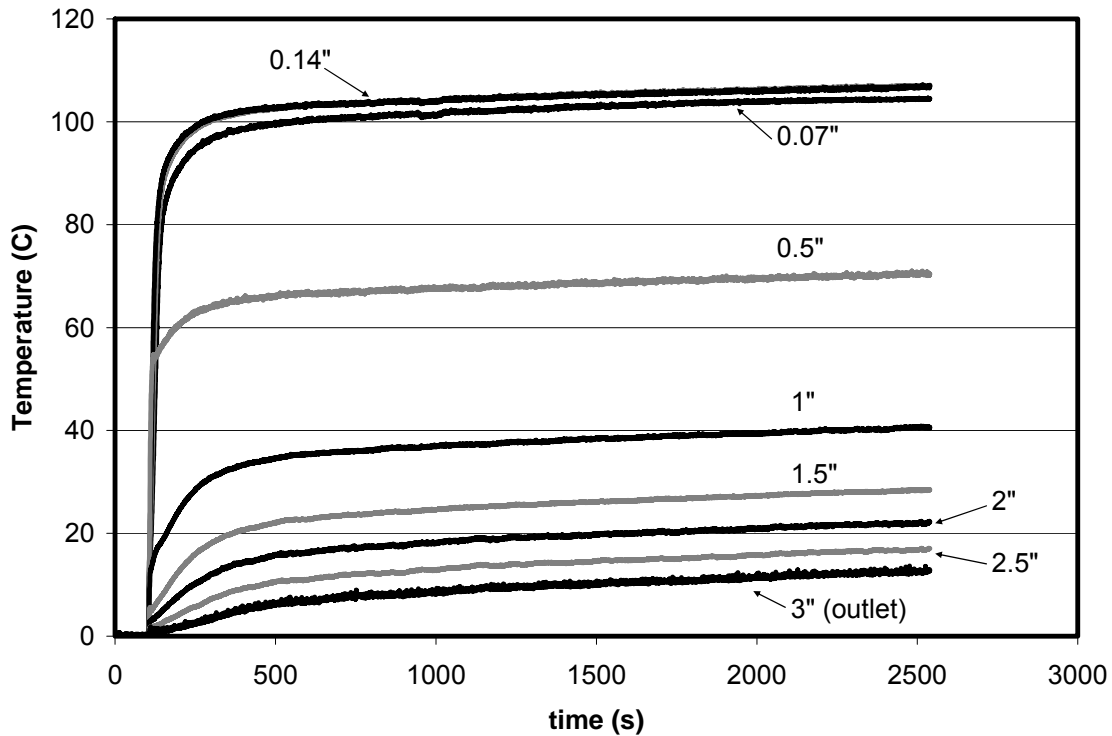
**Figure 4-20: Temperature profiles at nine positions during a steady-state propylene oxidation experiment with the aged catalyst sample.**

As with the test using the fresh sample, the inlet temperature was high enough to ensure complete oxidation near the inlet. With complete oxidation observed at the inlet, the temperature rises seen at downstream positions are attributed to heat carried away from the reaction zone via conduction and convection.

## 4.1.3.3.2 IR-Thermography Temperature Data Obtained During Temperature Programmed Oxidation

The same temperature ramp experiments described above were repeated with the catalyst aged at 675°C and the temperature profiles obtained are shown in Figure 4-21.
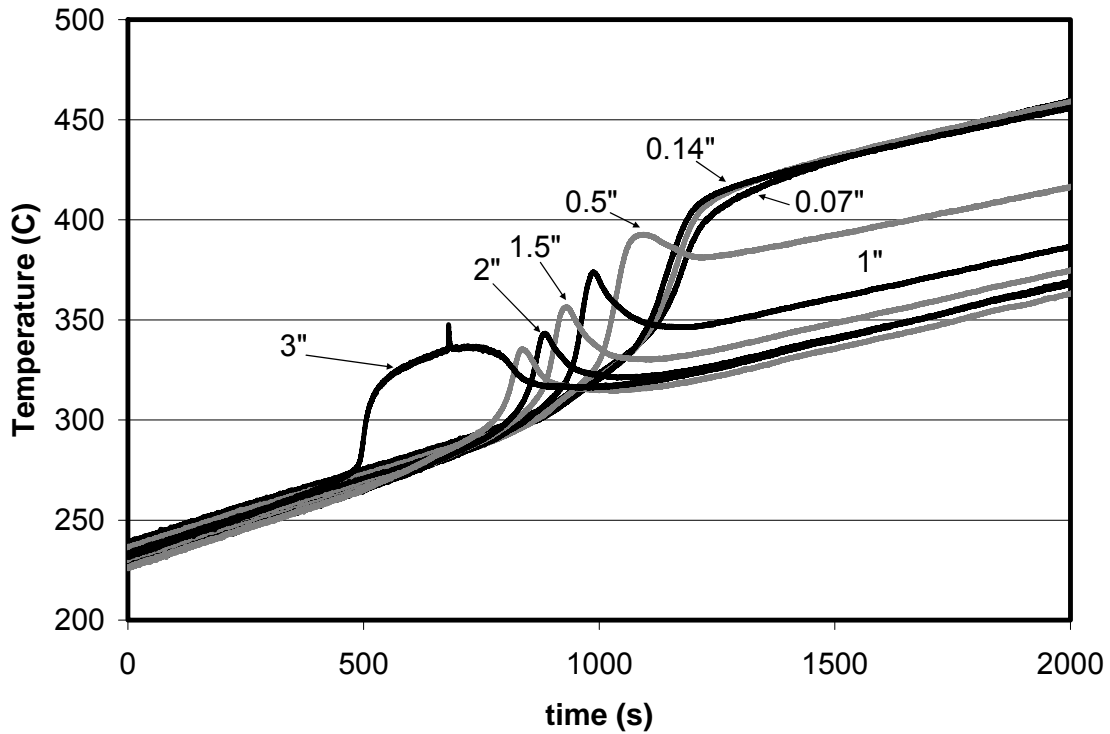
**Figure 4-21: Temperature profiles at nine positions during a ramped propylene oxidation experiment on the aged catalyst sample.**

Light-off over the aged sample initiated at the outlet position again, 3", but at a higher inlet temperature. The higher temperature is an indication that thermally aging the catalyst negatively impacted its propylene oxidation ability.

Again, the heater's contribution was subtracted, and Figure 4-22 is a graphical depiction of the procedure, the same as that in Figure 4-6. Note that the temperature ramp carried out was a new one that was again proven reproducible for the aged sample.
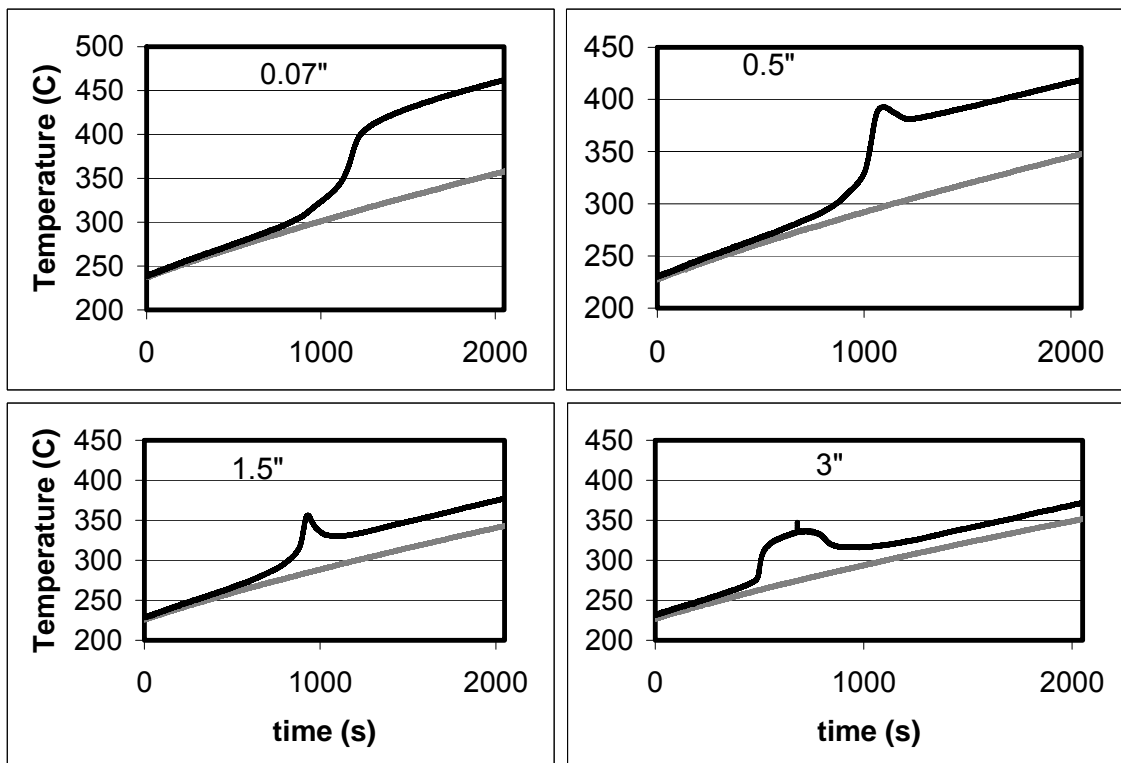
**Figure 4-22: The baseline temperature ramp data and the data obtained with reaction.**

The temperature profiles for the reaction over the aged catalyst after the heater baseline subtraction are shown in Figure 4-23 below.
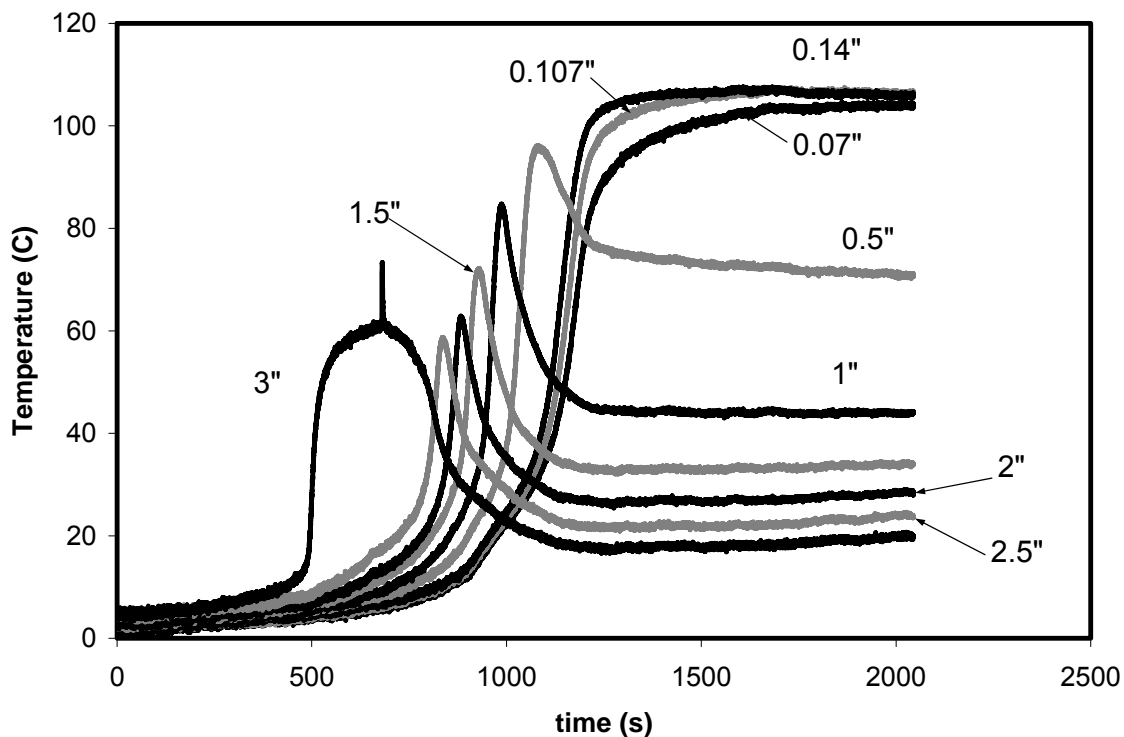
**Figure 4-23: Temperature profiles over nine positions for the aged sample, with the heater contribution removed.**

The maximum temperature rise obtained from the ramped propylene oxidation experiment was identical to the steady-state experiment, ~105°C. This provides further confidence in the validity of the conduction subtraction method.

To verify data reproducibility from the ramped propylene oxidation experiments over the aged catalyst, the experiments were repeated with select data plotted in Figure 4-24.
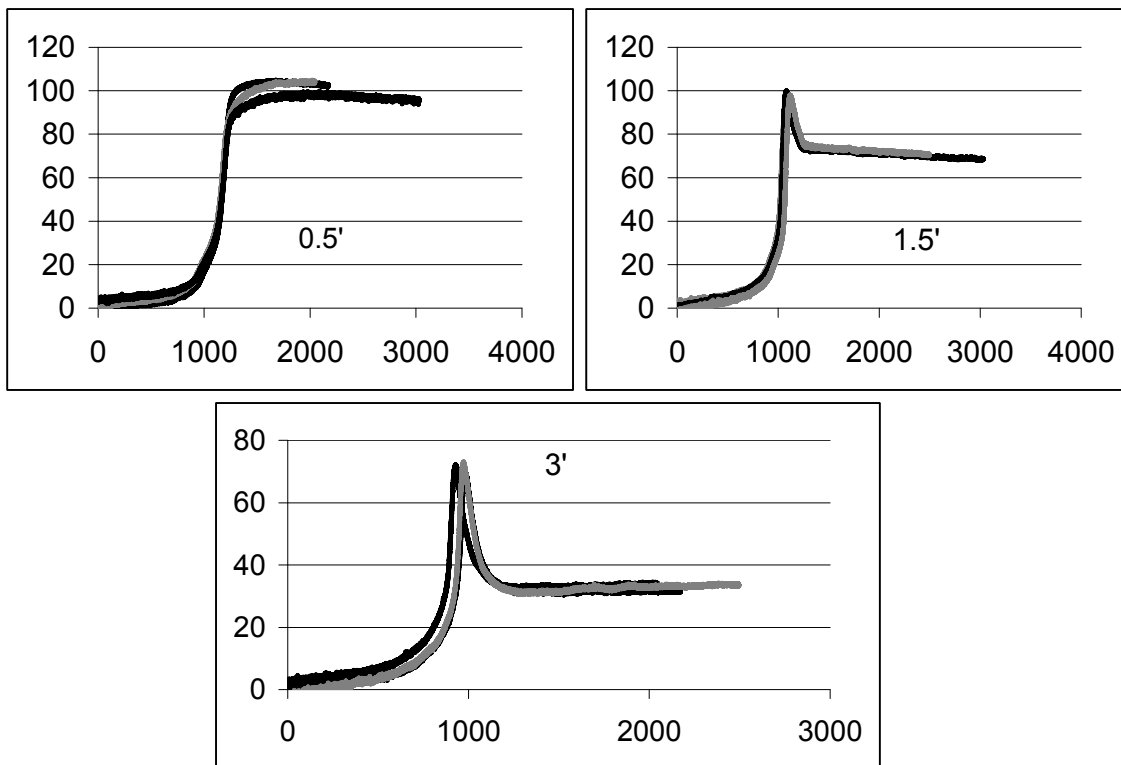
**Figure 4-24: Reproducibility check for the ramped propylene oxidation experiments with the aged sample. Three data sets from three positions are shown.**

The temperature profiles obtained after the temperature ramp associated with the furnace input had been removed as well as the conduction contribution (via a similar procedure used to make Figure 4-13 for the fresh sample) removed are shown in Figure 4-25.
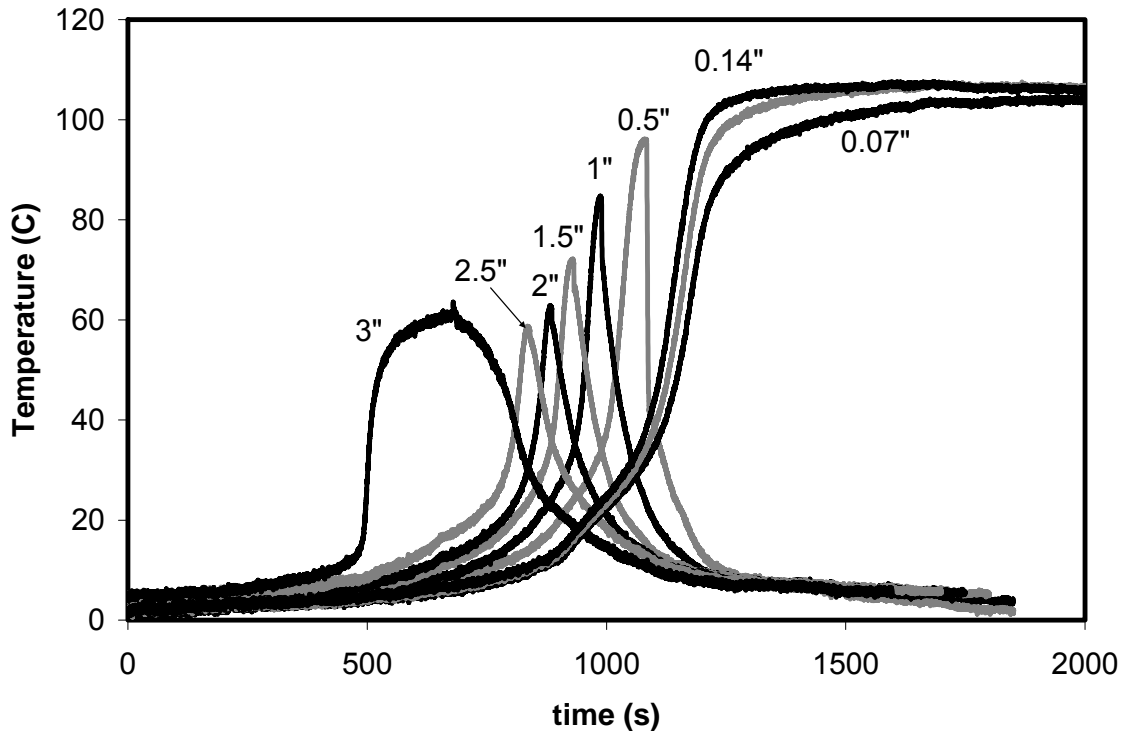
**Figure 4-25: Final temperature profiles showing the reaction heat effects alone, during a ramped propylene oxidation experiment over the aged catalyst sample.**

In comparing Figures 4-25 and 4-13, a key difference is that the peak temperature rises for the aged sample at downstream positions were higher. For example, at 3" from the inlet, the peak temperature rise for the aged sample was 57°C, compared to 40°C for the un-aged sample. At 2" from the inlet, the peak temperature rise for the aged sample was 59°C, where for the fresh sample it was 43°C. At positions further upstream, the differences in temperature rises between the fresh and aged samples decreased. At the 1" position, the temperature difference for the aged sample was 82°C, and 78°C for the fresh sample. At the very inlet, the maximum temperature rise for the aged sample was slightly less than that of the fresh sample, 103°C vs. 108°C for the un-aged sample. An increase in the temperature rise after thermal aging means that more reaction was occurring where the measurement was recorded. Therefore, at the downstream positions in the aged sample, more reactant was being oxidized at certain times compared with the fresh sample at the same location. Such amplification of the temperature excursions following

64

thermal deactivation has been previously observed [15,45]. Thermal aging of supported metal catalysts typically leads to metal crystallite growth, or sintering, and in greater segregation of the crystallites [48, 49]. Sintering typically leads to decreased catalyst activity due to fewer active sites exposed per volume of catalyst. Crystallite growth was confirmed by hydrogen chemisorption experiments with the fresh and aged samples as described in the experimental section. With the un-aged sample, reaction occurred from the inlet to the reaction front. With decreased activity due to sintering, less reaction occurs upstream of the reaction front, resulting in more reactant at downstream positions or at the reaction front position. Light-off occurs, but the reaction zone is more localized due to less upstream reaction, leading to the larger temperature rises at downstream positions observed after thermal degradation. This is possibly compounded by the fact that the active phase crystallites are further apart after thermal degradation, and therefore slower conduction, or heat transfer between the crystallites, occurs. Such has been suggested in previous thermography-based research [36]. Both effects lead to a more localized reaction zone at the outlet and beginning of oxidation or light-off, thus more reactant gets converted near the outlet and hence an increased temperature rise is observed.

## 4.1.3.3.3 Mass Spectrometer Concentration Data

The concentration profiles at five equidistant positions down the length of the catalyst are shown for the sample aged at 675°C as a function of time in Figure 4-26 and distance from the inlet in Figure 4-27.
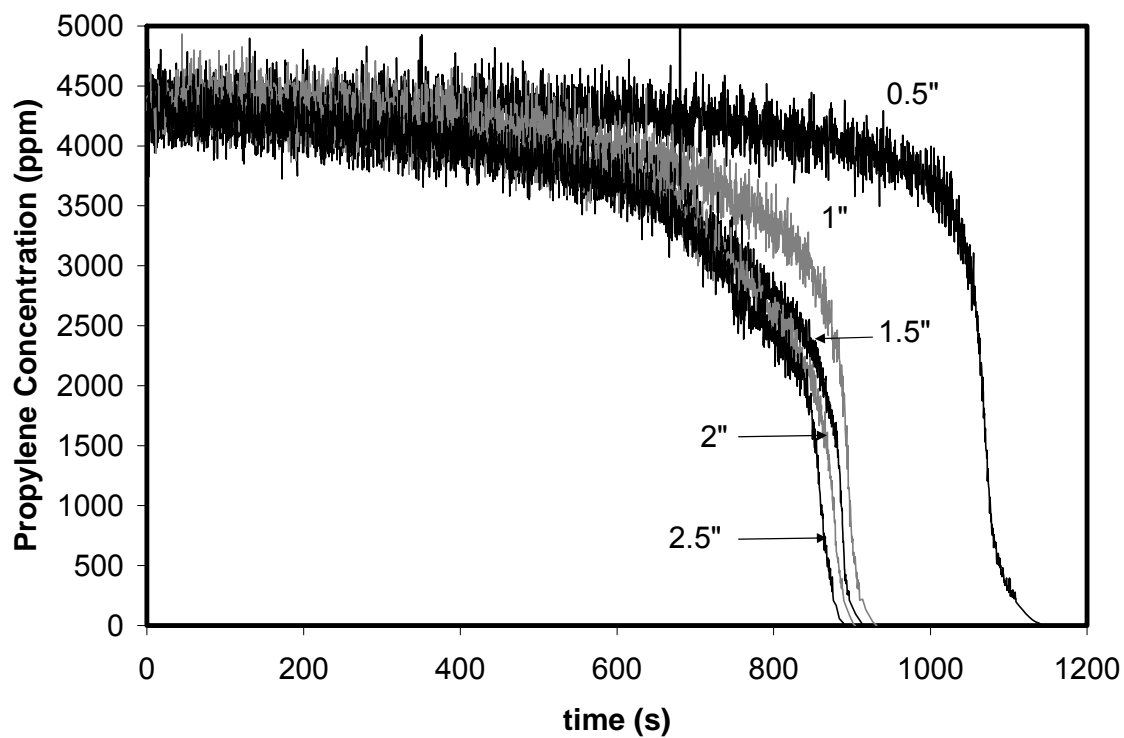
**Figure 4-26: Propylene concentration profiles at five equidistant positions during a ramped propylene oxidation experiment over the aged catalyst sample.**
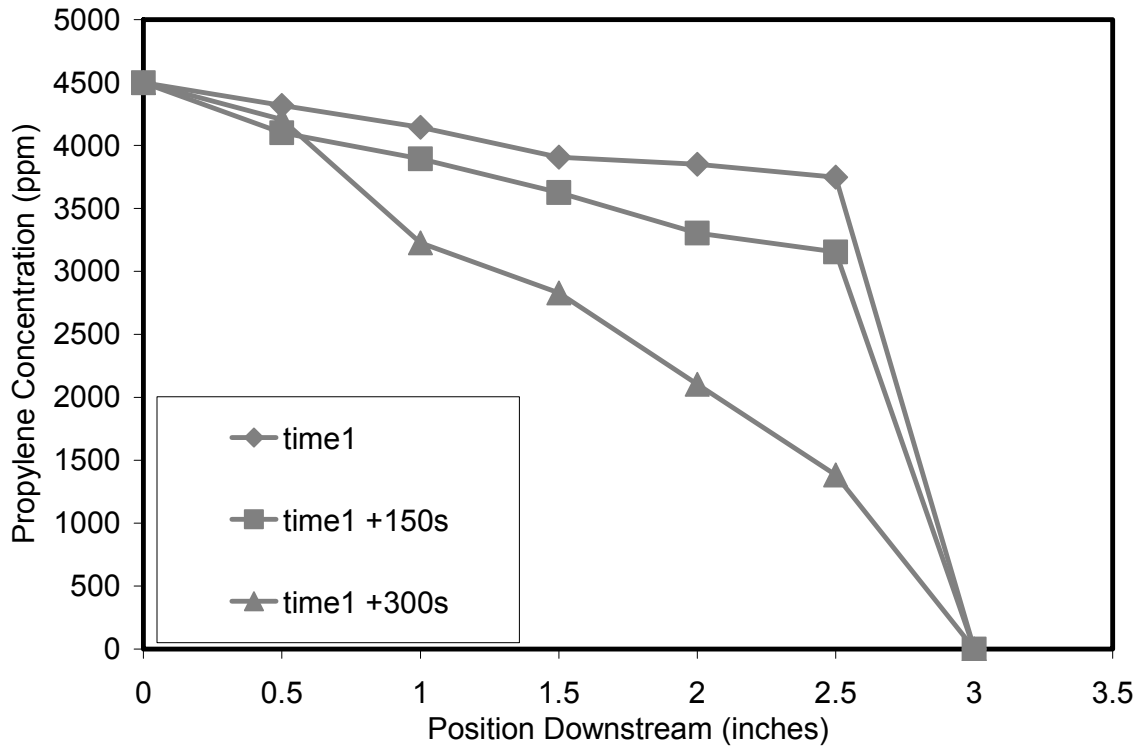
**Figure 4-27: Propylene concentration versus distance downstream from the inlet (inches) and time, for the ramped propylene oxidation experiment with the aged catalyst sample.**

The concentration profiles with the aged sample are steeper than those of the un-aged sample, comparing Figures 4-26 and 4-27 with Figures 4-16 and 4-19, indicating sharper gradients. According to the data in Fig 4-26, 42 seconds elapsed for the reaction front to travel from 2.5" to 1" (after the concentration reached zero at those positions), but ~ 5 times that to travel an extra 0.5" upstream.

These data indicate that at the onset of complete oxidation within the monolith, only the last 0.5" of the catalyst (i.e. between 2.5"-3") was used to achieve complete conversion, and that 300 s had to elapse (the third line) before the reaction zone spread over the entire monolith.

The data in Figures 4-26 and 4-27 imply that the reaction zone became more localized.

The two figures below are plots of the temperature rise profiles for the fresh and aged samples overlaid on two plots, showing trends at four positions.
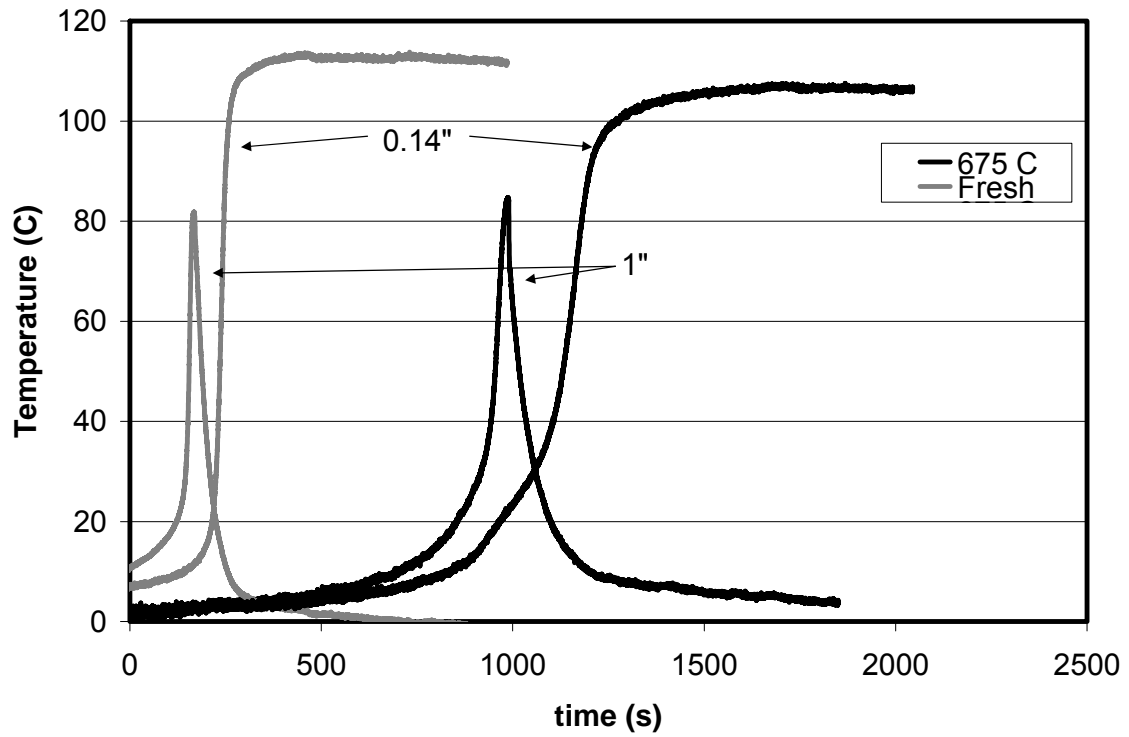


**Figure 4-28: Temperature profiles for two of the upstream positions lined up in time under the same inlet temperature for the fresh and aged samples.**
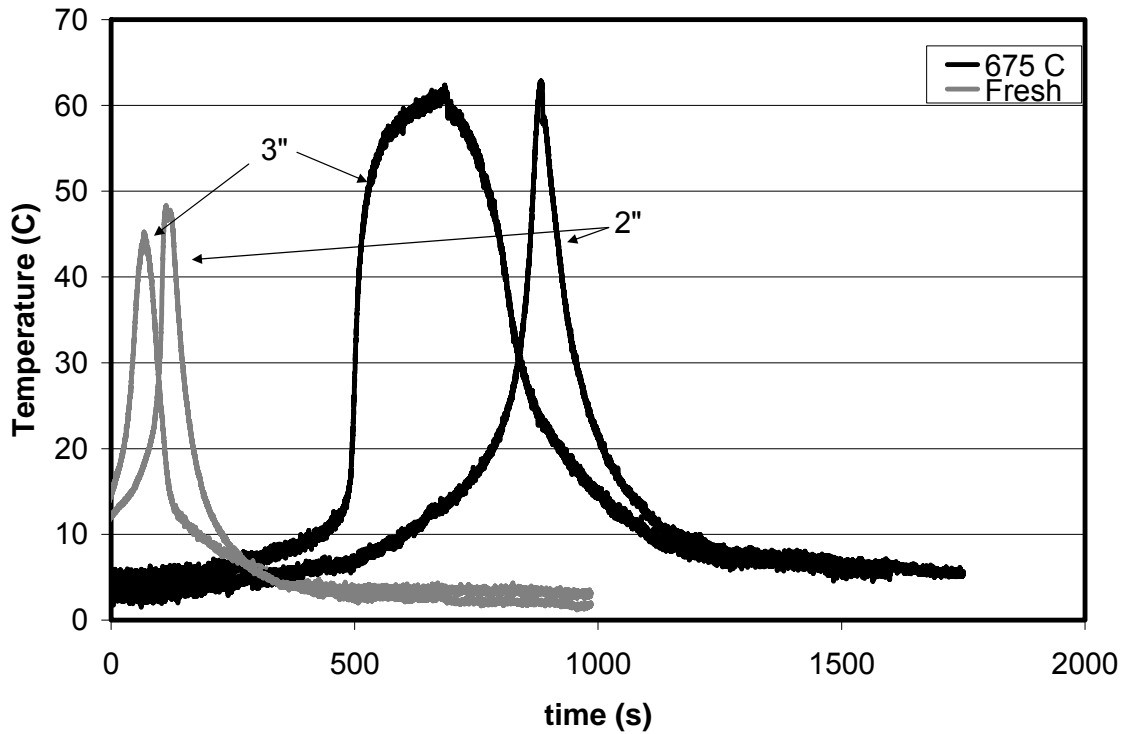
**Figure 4-29: Temperature profiles for two of the downstream positions lined up in time under the same inlet temperature for the fresh and aged samples.**

To line up the data shown in these two figures, time = 0 seconds was chosen when the inlet temperature was 176°C. The temperature rises at positions 3" and 2", Figure 4-29, are larger in magnitude for the aged sample than the fresh, by ~ 17°C. As the reaction front moved further upstream, the difference in temperature rise at 1" was reduced, and was almost identical when it settled at 0.14". As was discussed above, the increase in temperature rise for the aged sample at downstream positions is attributed to more reactant being converted at these positions. The source of this 'extra' concentration was not due to an increase in the amount being fed, but rather from upstream positions being less efficient, hence supporting the fact that the reaction zone became more localized.

## 4.2 Application of Concept – Comparing Fresh and Aged Samples

### 4.2.1 Narrower Reaction Zone

The temperature data discussed above indicated that more reactant was being consumed at downstream positions, with the amounts reacting in certain regions more equivalent at upstream positions. This is further highlighted in Figure 4-30, which is a plot of the propylene concentration profiles versus the distance downstream for the fresh and aged samples when the propylene concentration reached zero at four positions.
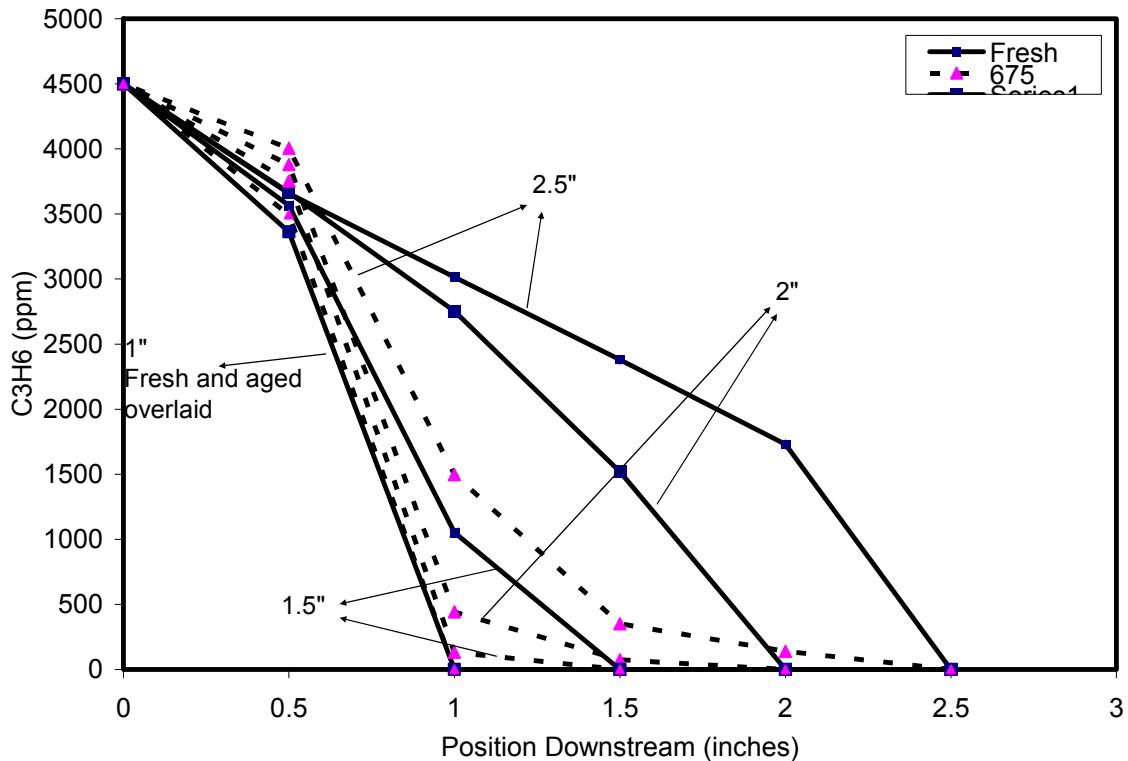


**Figure 4-30: Propylene concentration profiles at four positions for the fresh and aged catalysts, as a function of the downstream distance (inches) from the inlet. Each profile represents a point in time when the propylene concentration reached zero starting from the most downstream position 2.5".**

By the time the reaction front reached 2.5" (indicated by zero concentration) for the fresh sample, there was a gradient in concentration extending all the way from the inlet of the catalyst to 2.5". For the aged sample however, this reaction zone seemed to start after 0.5" (as seen by the steeper drop in concentration after 0.5") indicating that less was oxidized in the first 0.5" as compared with the fresh sample. This is identical to the conclusions obtained from the temperature profiles.

However, as shown in Figure 4-30, the difference in concentration gradients between the two samples was closer the further upstream the reaction front moved, again confirming the behavior seen from the temperature profiles in Figures 4-28 and 4-29, and the conclusion that the reaction front became narrower.

## *4.2.2 Slower reaction front*

A key observation is the increased time it takes for the reaction front to travel from the point of initiation at the sample outlet to the inlet of the catalyst. In Fig 4-31, the elapsed time between a position's temperature peaks and that of the most downstream position, is shown.
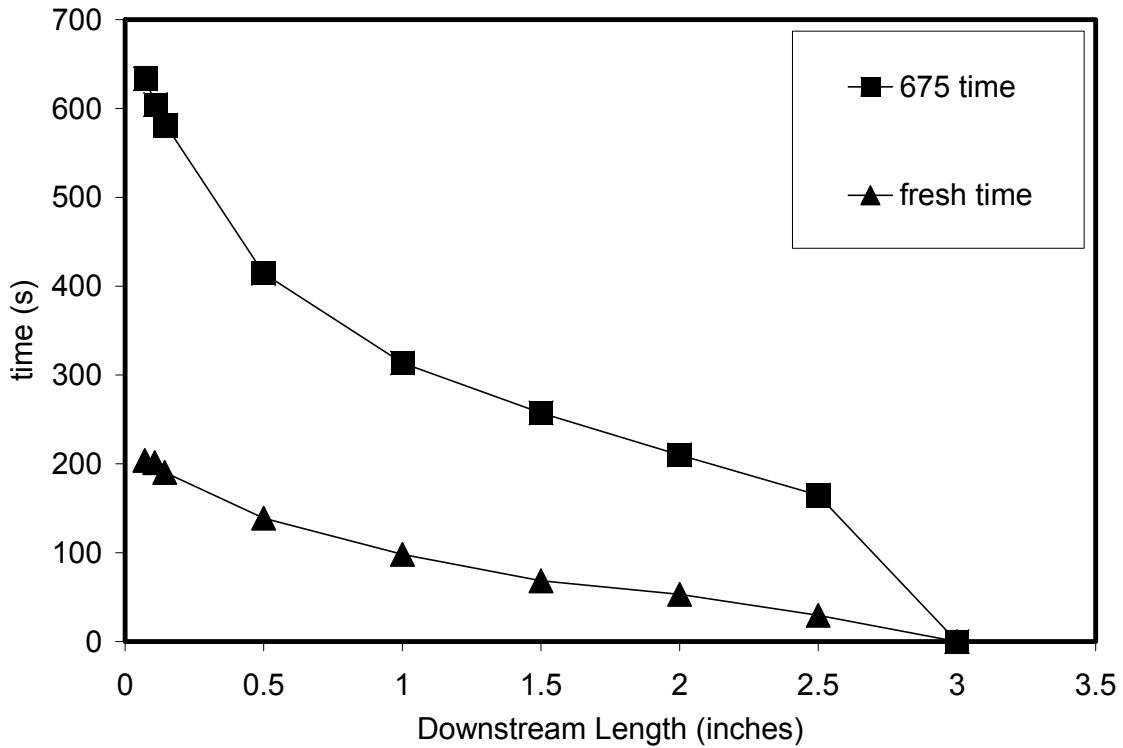
**Figure 4-31: Time for the reaction front to travel from the rear of the catalyst at 3" to different upstream positions for the fresh and aged catalysts.**

For the un-aged sample, the total time taken for the temperature wave to move from the back of the monolith until steady-state was achieved at the inlet region was ~ 200 s. For the sample aged at 675°C, this time was ~ 630 s. Similarly, after aging the sample at 750°C, data not shown, the time increased to ~ 1200 s. It is therefore apparent that the temperature propagation, and therefore the reaction front, moves more slowly after thermal degradation.

# Conclusions

IR-thermography and SpaciMS were used to evaluate concentration and temperature values over a Pt/Al$_2$O$_3$ monolith-supported catalyst during propylene oxidation before and after thermal degradation. Both techniques showed back-to-front light-off under the conditions tested. Once oxidation begins, thermography data show that there is significant conduction of heat along the monolith from upstream positions. The mass spectrometer data show that as the concentration dropped to 0 at a distinct position, the maximum temperature rise at that same position was observed. Although the thermography data were obtained with one experiment, they were complicated by conductive and convective heat transfer. However, using the SPACiMS data to confirm the reaction zone position allowed downstream removal of the heat from conduction or convection. Thermal degradation caused the ignition front to move significantly more slowly relative to the non-thermally degraded sample. The combination of the two techniques results in a clear picture of the reactant and product gas species and temperature distribution along the catalyst length.

# Recommendations

- Implement an automated/motorized mechanism to move the capillary within the reactor, to improve position accuracy.

- Install a cooling mechanism for forced cooling of the reactor to bring it from high to low temperatures in shorter times which will increase productivity.

- Implement a pneumatic valve switching mechanism that will decrease human intervention and fittings changes back and forth, hence minimizing the room for human errors and leaks occurrence.

- Program the IR-camera to have a wider calibration range for reactions with higher exothermic heat generation.

- Install more thermocouples along the heated lines for better temperature monitoring and control.

# References

1. H. F. Rase., Fixed-bed reactor design and diagnostics: gas phase reactions Boston: Butterworths, c1990

2. O. Levenspiel, Chemical reaction engineering, New York, Wiley, 1998, 3$^{rd}$ edition,

3. www.comsol.com/showroom/gallery/images/257_l.jpg

4. A. Jaree, H. Budman, R. Hudgins, P. Silveston, V. Yakhnin, and M. Menzinger, Catalysis Today 69(2001)137.

5. V. Tomasic, F. Jovic, Applied Catalysis A 311(2006)112.

6. V. Tomasic, Catalysis Today 119(2007)106.

7. K. Pangarkar, T. J. Schildhauer, J. Ruud van Ommen, J. Nijenhuis, F. Kapteijn, J. Moulijn, Industrial Engineering and Chemistry Research 47(2008)3720.

8. www.dieselnet.com

9. M. J. Bradley, B. M. Jones, Ambio 31-2(2002.)141.

10. S. S. Nadadur, C. A. Miller, F. K. Hopke, T. Gordon, S. Vedal, J. Vandenberg, D. L. Costa, Toxicological Sciences 100-2(2007)318.

11. K. Ramanathan, A. Gopinath, AIChE Journal 54-7(2008)11.

12. I. Nova, C. Ciardelli, E. Tronconi, D. Chatterjee, B. Bandl-Konrad, Catalysis Today 114(2006)3.

13. W. S. Epling, L. E. Campbell, A. Yezerets, N. W. Currier, J. E. Parks, Catalysis Reviews 46-2(2004)163.

14. J.-S. Choi, W.P. Partridge, W.S. Epling, N.W. Currier, T.M. Yonushonis, Catalysis Today 114(2006)102.

15. A. Jaree, R.R. Hudgins, H. Budman, P.L. Silveston, V. Yakhnin, and M. Menzinger, Chemical Engineering Science 58(2003)833.

16. D. Luss and M. Sheintuch, Catalysis Today 105(2005)254.

17. L. Hegedus, AIChE Journal 21(1975).

18. S.H. Oh and J.C. Cavendish, AIChE Journal; 35(1985)935.

19. V. Yakhnin and M. Menzinger, Chemical Engineering Science 57(2002)4559.

20. M. Sheintuch and I. Keren, Chemical Engineering Science 55(2000)1461.

21. K. Ramanathan, V. Balakotaiah and D.H. West, Chemical Engineering Science 58(2003)1381.

22. K. Ramanathan, V. Balakotaiah, and D.H. West, Industrial Engineering and Chemistry Research 43(2004)288.

23. A. Cybulski and J.A. Moulijn, Catalysis Reviews – Science and Engineering 36(1994)179.

24. G. Groppi, E. Tronconi and P. Forzatti, Catalysis Reviews – Science and Engineering 41(1999)227.

25. S. C. Bates, R. Carangelo, K. Knight, M. Serio, Review Science Instrumentation 64-5(1993)1213.

26. C. D. Cooper, Air Pollution Control: a design approach Prospect Heights: Waveland Press, c1994.

27. S.W. Allison, G.T. Gillies, Review Science Instrumentation 68 (1997) 2615.

28. Introduction to infra-red and raman spectroscopy, Colthup, Norman B., Boston: Toronto Academic Press, c1990.

29. Schmitz, A; Pawlicki, P.; Chemical Engineering Progress 83-2(1987)40.

30. G. Phillipou, M. Somani and D. Luss, Chemical Engineering Science 48(1993)2325.

31. B. Marwaha, D. Luss, AIChE Journal 48-3(2002)617.

32. B. Marwaha and D. Luss, Chemical Engineering Science 58(2003)733.

33. B. Pinkerton, D. Luss, Industrial Engineering and Chemistry Research 46(2007)1898.

34. S. Sundarram, D. Luss, Industrial Engineering and Chemistry Research 46(2007)1485.

35. J. C. Kellow, E. E. Wolf, Chemical Engineering Science 45-8(1990)2597.

36. F. Qin, E. E. Wolf, Chemical Engineering Science 49-24A(1994)4263.

37. F. Qin, E. E. Wolf, Industrial Engineering and Chemistry Research 34(1995)2923.

38. B.H. West, S.P. Huff, J.E. Parks, S.A. Lewis, J.-S. Choi, W.P. Partridge, and J.M. Storey, SAE Technical Paper 1(2004)3023.

39. W.P. Partridge, J.M.E. Storey, S.A. Lewis, R.W. Smithwick, G.L. DeVault, M.J. Cunningham, N.W. Currier, and T.M. Yonushonis, SAE Technical Paper 1(2000)2952.

40. J.-S. Choi, W. Partridge, and C.S. Daw, Applied Catalysis B: Environmental 77(2007)145.

41. T. J. Toops, D. B. Smith, W. P. Partridge, Catalysis Today 114(2006)112.

42. J-S. Choi, W. P. Partridge, J. A. Pihl, C. S. Daw, Catalysis Today 136(2008)173.

43. R. Horn, K. A. Williams, N. J. Degenstein, L. D. Schmidt, Journal of Catalysis 242(2006)92.

44. G. J. Panuccio, L. D. Schmidt, Applied Catalysis A 332(2007)171.

45. V. Z. Yakhnin, M. Menzinger, AIChE Journal 44-5(1998)1222.

46. D. Luss, Industrial Engineering and Chemistry Research 36(1997)2931.

47. A. Jaree, M. Menzinger, V. Yakhnin, P.L. Silveston, and R.R. Hudgins, Chemical Engineering Science 59(2004)4011.

48. H.C. Yao, P. Wynbliatt, M. Sieg and H.K. Plummer, Jr., Plenum Press, New York, (1980)561.

49. R.T.K. Baker, C.H. Bartholomew and D.B. Dadyburjor, in J.A. Horsley (Editor and Project Leader), Mountain. View, 1991.

50. H. D. Minh, H. G. Bock, S. Tischer, O. Deutschmann, AIChE Journal 54-9(2008)2432.

51. H. Songling, L. Luming, Y. Haiqing, S. Keren, Proceedings Of SPIE 5046(2003)219.

52. P. P. Pescarmona, J. C. van der Waal, I. E. Maxwell, T. Maschmeyer, Catalysis Letters 63(1999)1.

# Appendix A

## *A-1 Mass Spectrometer Calibration Formula:*

50 mls of helium were added to the inlet stream, for a concentration of 0.66%, as an internal standard to be used in calculating other species concentrations.

$$He \ (input) = He \ (output) = (He\%) = 0.66\% \qquad \text{(a)}$$

A ratio between the partial pressures of He and the other chemical species was then calculated. $CO_2$ will be used as an example to illustrate the calculation.

$$Ratio = CO_2 \ (torr) \ / \ He \ (torr) \qquad \text{(b)}$$

The uncorrected species percentage calculation was then obtained by multiplying the known He percentage entering the system, the basis, with the ratio. This provided the initial percentage of the chemical species in question.

$$CO_2 \ \%(1) = \ He(input) * Ratio \qquad \text{(c)}$$

The calculation did not take into account the relative sensitivity of the chemical species with the detector in question. Thus a multiplier (M) was required to correct for this either inflation or deflation of partial pressure observed.

$$CO_2 \ \%(2) = M * CO_2\% \ (1) \qquad \text{(d)}$$

A final correction factor (C) was also required. The partial pressure observed at any amu was never zero. The mass spectrometer could identify positive or negative torr values when no gas at that amu was present depending once again on the reaction that occurred with the detector. Thus due to the linear shift, a y intercept was required.

$$CO_2\% = CO_2 \ \%(2) + C \qquad \text{(e)}$$

The entire equation developed, with $CO_2$ as an example here, was therefore:

$$CO_2\% = M * (He\%) * [CO_2 \text{ (torr)} / He \text{ (torr)}]) + C \qquad (f)$$

## *A-2 Calibration Curves:*

From equation (f) above, the multiplier and the constant are parameters that fit a straight line equation. Hence, to achieve the best fit values for the parameters, a calibration had to be carried out where a number of points at which the exact concentration of the species in question was known, versus the uncorrected percentage obtained from the mass spectrometer. The curves were generated, and were proven to indeed follow a linear relationship.

## A-2.1 Oxygen

Due to the inability of the MKS FTIR analyzer to detect $O_2$, it was very important that the mass spectrometer be calibrated to determine the percent composition of $O_2$. Using pure $N_2$ as the carrier and the 50 mls of He within the flow as a tracer the calibration was accomplished.

A known, metered percentage of $O_2$ was put into the system via the mass flow controllers, and the mass spectrometer scanned for 32 (oxygen) and 4 (helium). From the known amount of $N_2$, and thus He % into the system, an initial estimate of $O_2$ is identified. From this a calibration is developed, where a linear relationship is observed relating the observed initial percentage and the known percentage based on the input flow. From the best fit line, both the multiplier and correction factor could be determined.

Figure A-1 below is a plot of the data and the best fit line of the oxygen percentage versus the mass spectrometer percentage. The equation obtained is shown on the plot.
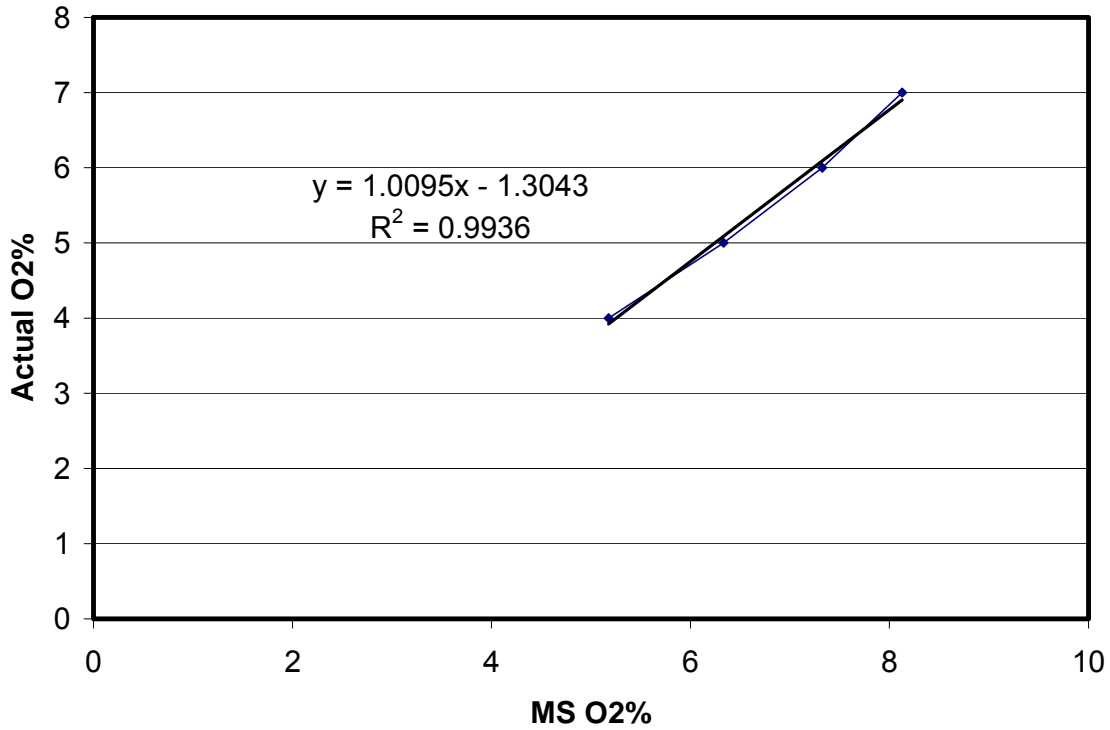


**Figure A-1: Mass spectrometer calibration line for oxygen.**

From the equation of the best fit line, it was found that the multiplier had a value of M = 1.0095, and the constant was C = -1.3043.

## A-2.2 Propylene, Carbon Dioxide and Water

The MKS FTIR could measure $CO_2$, $H_2O$ and $C_3H_6$, so to calibrate the flow rates; the ratio obtained from the mass spectrometer was compared to the MKS readings instead of the flow controllers. This provided a higher accuracy as the flow controllers were not

exact between 5 and 95% of their range. The calibration lines for propylene and carbon

dioxide are shown in Figure A-2 and A-3 below.



$$y = 1.3346x - 72.746$$
$$R^2 = 0.9998$$
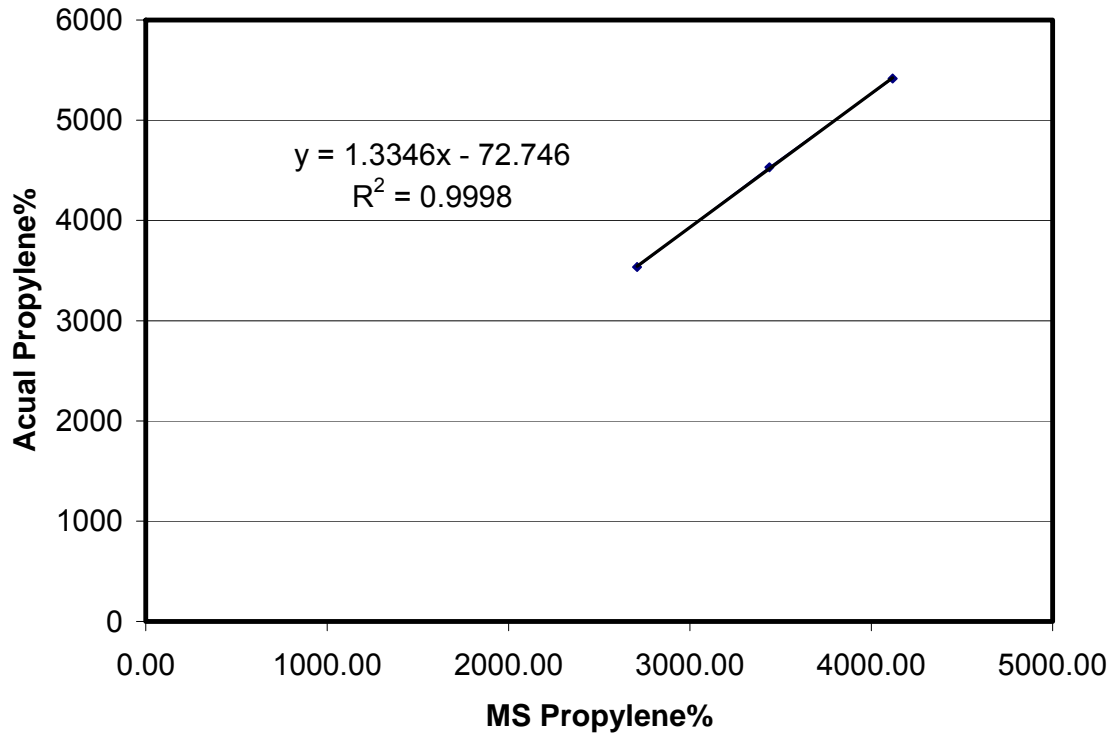
**Figure A-2: Mass spectrometer calibration line for propylene.**

$$y = 0.81x - 0.0876$$
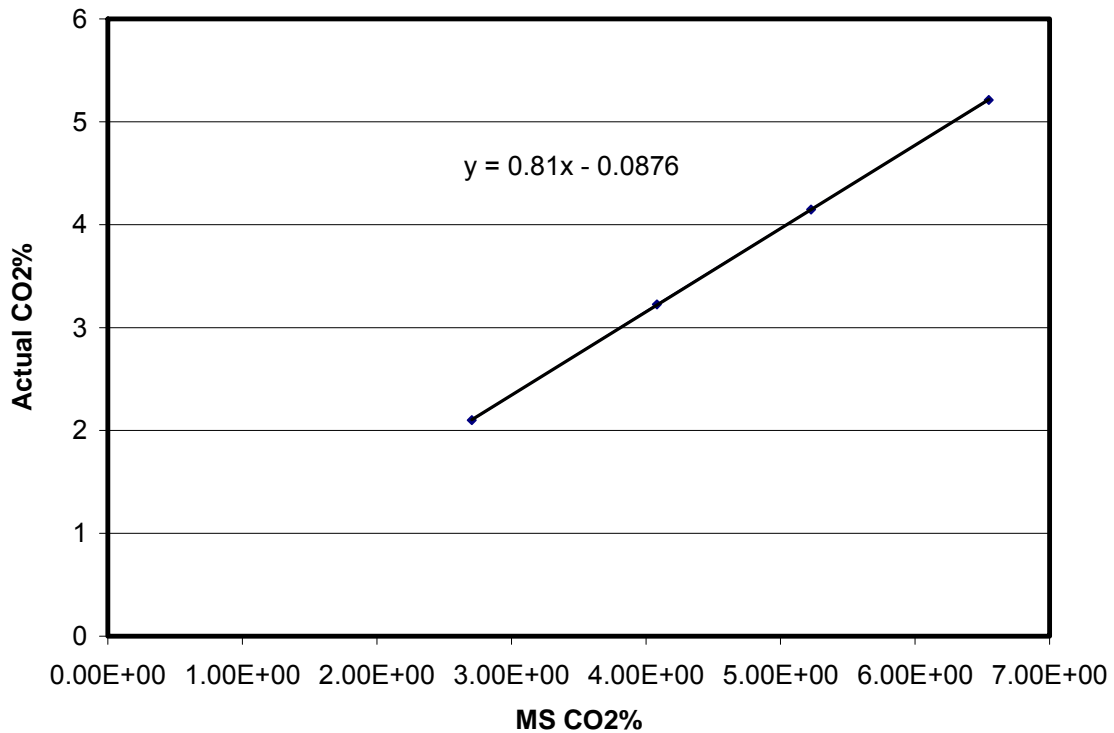
**Figure A-3: Mass spectrometer calibration line for carbon dioxide.**

Again the multiplier and constant were found from the best fit line equations shown on the graphs.

After proving that the mass spectrometer calibration followed a linear relationship, it wasn't necessary to run a separate calibration after every experiment with multiple data points. Rather, only two points generated from the experimental data were sufficient. The first point was the known upstream inlet gas concentration, and the second point was the downstream concentration from the FTIR analyzer. The calibration for $H_2O$ shown in Figure A-4 below is an example of how this was done.
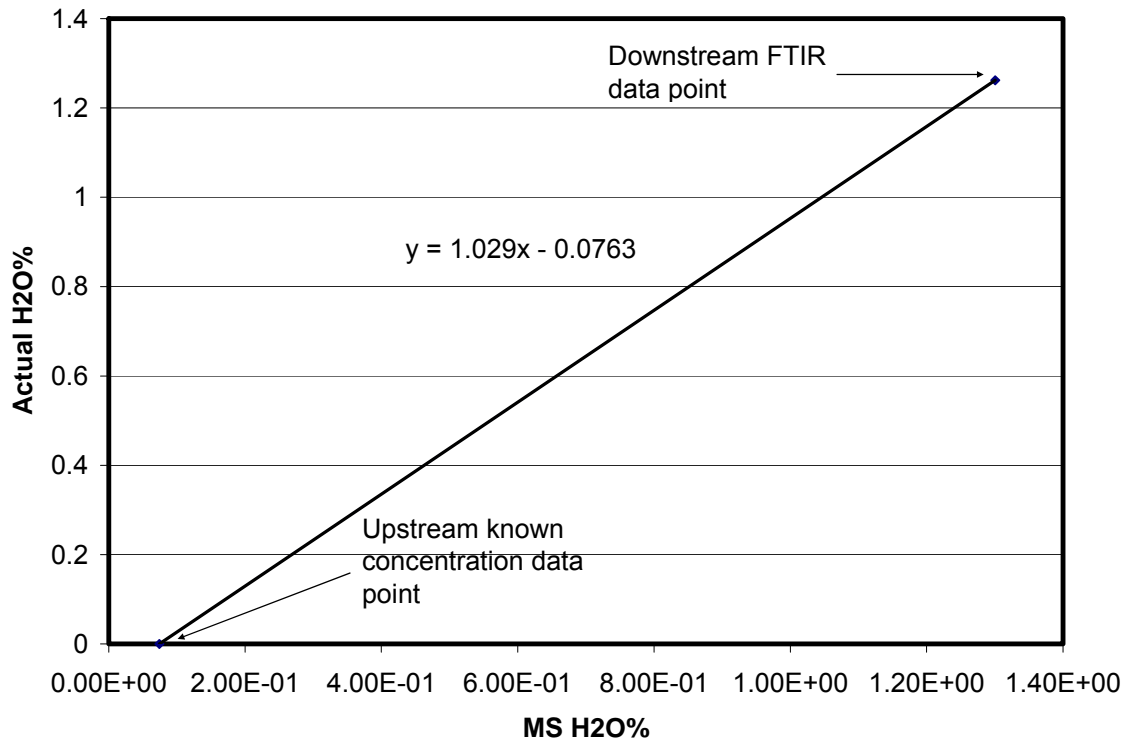
**Figure A-4: Mass spectrometer calibration line for carbon dioxide.**